VOL 102 No 2
June 2011

SAIEE Africa Research Journal

SAIEE AFRICA RESEARCH JOURNAL EDITORIAL STAFF ..... IFC
GUEST EDITORIAL.....30

Determining the Feasibility of Measuring Outdoor Road Cycling Kinematics Using Inertial Motion Capture Technology
by J. Cockcroft and C. Scheffer.....31

The Electro-Thermal Properties of Integrated Circuit Microbolometers
by M. du Plessis, J. Schoeman, W. Maclean and C. Schutte 40

Investigation into a Multilateration Laser Tracking System for the National Metrology Institute of South Africa
by G.P. Greeff and O.A. Kruger.....49

Notes for authors.....IBC

GUEST EDITORIAL

YOU CANNOT CONTROL WHAT YOU CANNOT MEASURE

Measurement science and technology, remains at the centre of the study and development of the world around us for man's benefit. Lord Kelvin once said that: "When you can measure what you are speaking about and express it in numbers, you know something about it; but when you cannot measure it, when you cannot express it in numbers, your knowledge is of a meagre and unsatisfactory kind: it may be the beginnings of knowledge but you have scarcely in your thoughts advanced to the stage of Science." Such scientific measurement extends man's inbuilt senses, it enables us to operate our modern industry, safeguards our health and improves our quality of life. This is also a well-established knowledge field in engineering and specifically electrical engineering, with the IEEE Instrumentation and Measurement Society for example over 60 years old.

The development and characterisation of new measurement technology is as important as ever and South Africa should play a continuing role in this field if it is to remain relevant in the modern world. One forum where such work is discussed is at the Test and Measurement Conference, which was held in November 2010 in the central Drakensberg. This conference is organized by the National Laboratory Association. The work of the metrology, industrial test and measurement and academic measurement technology communities was showcased. The conference spans all measurement domains; that is chemical, electromagnetic and mechanical. This special issue showcases some of the most exemplary papers from the conference, falling in the physical measurement domains. The highest quality conference contributions were panel-selected via the conference structures and invited to submit updated versions for the Africa Research Journal, where-after a normal peer review process was followed.

The next Test and Measurement conference takes place in 2012; please keep a lookout for the announcements. The National Metrology Institute of South Africa (NMISA), and the Department of Trade and Industry also sees it as important to support this forum. The NMISA is amongst other things responsible for maintaining the SI units and to maintain and develop primary scientific standards of physical quantities for South Africa and compare those standards with other national standards to ensure global measurement equivalence, and is therefore also involved in the R&D of advanced measurement methods and technology in this context.

We look forward to seeing more players involved in the next round, and hope that you enjoy the articles from last year's conference!

Dr Johan Burger
National Metrology Institute of South Africa

DETERMINING THE FEASIBILITY OF MEASURING OUTDOOR ROAD CYCLING KINEMATICS USING INERTIAL MOTION CAPTURE TECHNOLOGY

J. Cockcroft* and C. Scheffer**

** Biomedical Engineering Research Group, Dept. of Mechanical and Mechatronic Engineering, Stellenbosch University, Stellenbosch, South Africa E-mail: johnc@sun.ac.za*
*** Biomedical Engineering Research Group, Dept. of Mechanical and Mechatronic Engineering, Stellenbosch University, Stellenbosch, South Africa E-mail: cscheffer@sun.ac.za*

Abstract: Unlike traditional optical systems, inertial motion capture systems (IMSs) can measure human kinematics outdoors as well as in a laboratory. However, these systems are sensitive to magnetic interference. This study evaluated an IMS for use in sports performance analysis, using road cycling as a case study. The objective was to establish the feasibility of obtaining accurate outdoor kinematic data on competition-level road bicycles. Ten male cyclists were recorded on their own bicycle on a stretch of road wearing the IMS. Results revealed unacceptable magnetic interference to the IMS near the pedal and handlebar interfaces. Therefore, accurate full-body cycling kinematics is not currently feasible on most competition-level road bicycles. However, lower limb flexion measurements are possible using the IMS's kinematic coupling algorithm which obtained RMS errors of less than 3.5° for all joints in a benchmark test with an optical system regarded as gold-standard.

Keywords: Motion capture, road cycling, kinematics, MVN, inertial systems

1. INTRODUCTION

1.1 Background

Motion capture (Mocap) is the process of measuring and digitally reproducing the motion of an object. Mocap of human movement involves individually tracking several strategic anatomical landmarks in space using motion sensors. These landmarks are used to estimate full-body kinematics using a biomechanical model consisting of several rigid body segments joined together by joints. The Mocap data can then be reviewed visually on a computer screen using an avatar or numerically for quantative analysis of segment kinematics and joint angles.

Mocap was first utilized in the 19th century, when it was employed in military programs to improve the mobility of troops [1]. However, it was only after the Second World War when there was a need for improved prosthetics and treatment for war veterans that the foundational studies were conducted in human locomotion by Eberhart and Inman [2]. Later, with the advent of computer processing, more sophisticated Mocap systems were developed. State-of-the-art Mocap systems, which utilize various different types of sensor technology, now provide full-body Mocap data in 3D and at sample speeds of several hundred and even thousand frames per second. Mocap is employed in a variety of fields today. For example, it is used in the entertainment industry for creating realistic animations in games and movies and for evaluating workplace ergonomics in industry [3]. It also provides accurate and comprehensive kinematic measurements for movement sciences research such as for gait analysis [4].

Optical Mocap systems such as the Vicon (Oxford Metrics Ltd.), which use advanced camera systems to track markers attached to the subject, are currently considered the gold-standard technology. However, due to significant advances made over the last two decades in the design and manufacture of micro-electromechanical systems (MEMS), an alternative Mocap technology has emerged: inertial Mocap systems (IMSs). IMSs track human motion using MEMS inertial measurement units (IMUs), which are compact sensor modules containing tiny accelerometers and gyroscopes, and magnetometers. IMU's are widely employed in inertial navigation systems (INSs) for aerospace, aviation, naval and ground transportation applications, as well as for robotics control. The major advantage of IMSs over the Vicon systems is their portability, since optical Mocap is generally restricted to laboratory use [5]. Furthermore, optical Mocap generally requires line of sight, good lighting conditions and significant post-processing [6]. IMSs are also significantly more affordable, quicker to set up and easier to use. However, one drawback of IMSs is that they are sensitive to prolonged magnetic interference, due to the use of magnetometers in the IMUs.

1.2 Motivation and objectives

Since optical systems have been the traditional benchmark in Mocap technology, almost all studies conducted using Mocap have been restricted to laboratory-based experiments. This has severely limited the scope of Mocap research performed in the field of sports science. However, for many sporting codes, IMSs are ideal for measuring an athlete's technique in their competitive arena instead of in a simulated laboratory environment. Therefore, the prospect of using an IMS for field-based Mocap holds great promise for more realistic experimental data. With insights gained from IMS field data, numerous improvements could be made to training

routines, injury prevention programs and performance optimization initiatives. However, although IMSs have already become extremely popular in the entertainment industry and have been validated for clinical studies [7, 8], they have not yet been readily adopted for sports science research. Therefore, the objective of this study was to determine the feasibility of using an IMS, the MVN BIOMECH system developed by Xsens B.V. (Enschede, Netherlands), to measure outdoor road cycling kinematics. The first potential obstacle which needed to be evaluated was measurement error caused by possible magnetic interference to the MVN from ferromagnetic materials in road bicycles.

2. DATA COLLECTION

2.1 The MVN BIOMECH system

The MVN system is stored in a portable suitcase, as shown in Figure 1a. It consists of 17 IMUs (Figure 1b), contained in a body-fitting Lycra suit (Figure 1c) which fixes the IMUs on strategic body segments to measure their individual kinematics. Two wireless onboard transmitters synchronize the IMU data signals and relay them to a nearby computer via USB receivers (Figure 1d). The MVN software then uses advanced sensor fusion techniques and a biomechanical model to digitally reproduce the full-body motion of the human subject. This is summarized in a whitepaper by Xsens [9].

Each IMU contains a triaxial accelerometer, gyroscope and magnetometer which together measure the IMU's global kinematics. The IMU data signals, which can be sampled at speeds ranging from 60-120 Hz, are used as inputs into an INS to track the motion of all 17 IMUs. Integration of the accelerometer and gyroscope measurements provides local linear and angular position, velocity and acceleration while the magnetometers are used as a compass to obtain heading in the global frame. Using pre-test calibration poses to obtain sensor-to-segment orientations the INS can then estimate the kinematics of an assigned rigid body segment for each IMU. The MVN software then assembles all the body segments together using a biomechanical model. The biomechanical model consists of 23 rigid segments connected by 22 joints, and is scaled anthropometrically to fit the physical dimensions of the test subject. By estimating the joint centre locations between the segments at each time step, the MVN system can then calculate the subject's full-body kinematics.

The MVN uses a recursive error-state Kalman filter to reduce measurement errors in the IMU sensors during the various stages of the Mocap process. In the INS, gyroscopic drift due to integration error is compensated for by the Kalman filter using sensor fusion. Drift in the horizontal plane is corrected using the heading data from the IMU magnetometers. Similarly, the accelerometers can be used as inclinometers to stabilize the gyroscopes in the vertical plane. Furthermore, accelerometer drift is addressed later in the biomechanical model using joint angle constraints and estimated contact points with the external world (such as feet on the ground). Lastly, advanced Kalman filtering is employed to reduce magnetic interference to the magnetometers caused by the close proximity of ferromagnetic materials or local magnetic fields. A more detailed treatment of the MVN operational principles is given by Roetenberg [10].

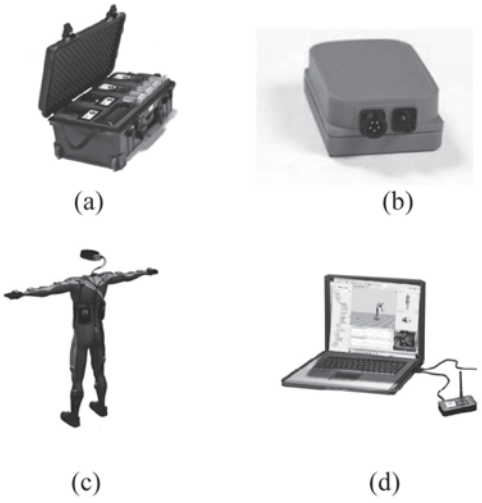

Figure 1: The MVN (a) suitcase (b) IMU (c) Lycra suit and (d) wireless transmitters and laptop (Source: Xsens)

2.2 Participants

Ten male cyclists were recruited for testing, all of which had competed regularly in professional races in the same season in which the testing was conducted. The cyclists used their own bicycles for the tests. Ethical approval was obtained for the testing and each subject granted informed consent to participate in the study.

2.3 Trial testing

The participants completed an indoor and outdoor test consisting of a one minute recording during steady state pedalling in a self-selected upright handlebar position at a constant cycling power of 3.5 $W.kg^{-1}$, which was used as an approximate medium intensity effort typical for competitive road cycling in another study [11]. The indoor test was conducted in a laboratory on a Powerbeam Pro stationary bicycle trainer (Figure 2a). The outdoor tests were conducted on a flat, straight stretch of open road (Figure 2b), with a pursuit vehicle carrying the laptop and receivers following within wireless range (~50 m). Each subject completed the tests on their own bicycle.

The basic sequence of the tests is shown in Figure 3. The suit setup included selecting the correct suit size and inserting and connecting the IMUs correctly. Secondly, the biomechanical model was scaled according to the subject's anthropometric dimensions. After this, the sensors-to-segment orientation was determined by the

two static calibration poses and two dynamic calibration movements. The subject then completed a warm up on the bicycle at 2 W.kg^{-1} for 3 minutes. Finally, the MVN recording was taken of the cyclist performing the test.

(a)

(b)

Figure 2: MVN recordings carried out (a) indoors on a trainer and (b) outdoors on the open road

After completing each recording, the MVN file was preprocessed in the MVN Studio software. This included reprocessing the file with the correct Kalman filter settings and editing the recording to isolate the desired period of the test. The raw magnetometer data for each IMU was then exported from the MVN software in XML format and imported into Matlab (Mathworks, Inc.) for data analysis.

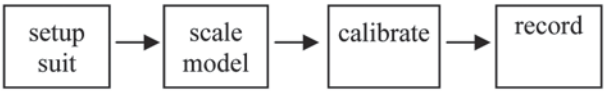

Figure 3: Main steps in test protocol

2.4 KiC benchmark test

Besides the default Kalman filter, which provides full-body kinematics without immunity to prolonged magnetic interference, the MVN system can also be operated with an alternative filter setting called Kinematic Coupling (KiC) [12]. The KiC algorithm calculates flexion angles for the hip, knee and ankle joints without the magnetometer data, making it immune to all magnetic disturbances. In order to evaluate the accuracy of the KiC data, a benchmark test was conducted with the gold-standard Vicon optical Mocap system. A single cyclist was recorded simultaneously with the MVN and Vicon systems (using the Plug-In Gait model) for one minute at 3.5 W.kg^{-1} on the Powerbeam trainer in order to compare the flexion measurements.

3. DATA ANALYSIS

3.1 Magnetic data

In order to evaluate the accuracy of MVN kinematic data it was necessary to quantify the magnetic interference caused by ferromagnetic bicycles components. This was done by determining the homogeneity of the local magnetic field measured by the IMUs. Two magnetic field parameters were used to do this. The first was the magnetic field intensity, which represents the density of the flux lines in the field. The second was the magnetic field inclination angle, which is the angle of the magnetic field relative to the global horizontal. The field intensity M_t was calculated for each IMU as in Equation 1.

$$|M_t| = \sqrt{m_{x,t^2} + m_{y,t^2} + m_{z,t^2}} \quad (1)$$

where $m_{x,t}$ $m_{y,t}$ and $m_{z,t}$ are normalized components of the magnetic field measurement within the local x-y-z coordinate system of each IMU's magnetometer. The scalar magnitude M_t was plotted as a function of time to identify changes in magnetic field intensity as a function of position for the moving IMUs on the lower limbs. Furthermore, intensity readings from stationary sensors on the upper body were compared to undisturbed field strength readings to determine the level of interference.

$$A_t = a_{x,t} + a_{y,t} + a_{z,t} \quad (2)$$

Similarly to the magnetometer data, the IMU accelerometer signal is represented by Equation 2. Since the inclination angle of the magnetic field is defined by the global horizontal, it therefore cannot be obtained directly from the IMUs local measurements because the orientation of the IMU in the global frame is unknown. However, when the IMU is stationary the accelerometer can be used as an inclinometer (by measuring the gravitational acceleration vector *g*) to determine the global vertical, and thus the perpendicular global horizontal, to rotate the IMU data measured in the local coordinate system to the global axis.

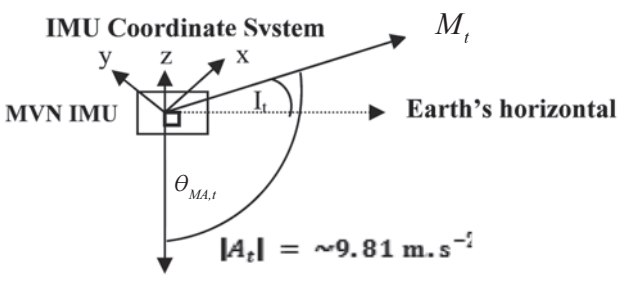

Figure 4: Inclination angle relative to M_t, A_t and the IMU

The angle between the magnetic field vector and gravitational acceleration vector can be calculated using the cosine rule as in Equation 3 (Figure 5).

$$\theta_{MA,t} = \cos^{-1}\left(\frac{|MA_t|^2-|M_t|^2-|A_t|^2}{-2|M_t||A_t|}\right) \quad (3)$$

where $|M|$ and $|A|$ represent the magnitude of the magnetic field intensity and approximate gravity vector respectively and are the two sides of the triangle adjacent to the angle $\theta_{MA,t}$.

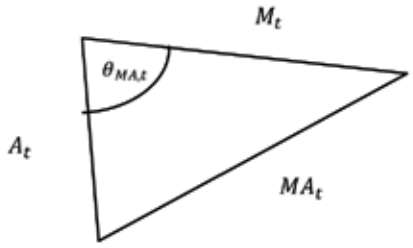

Figure 5: Cosine rule method used to calculate $\boldsymbol{\theta_{MA,t}}$

The third side of the triangle, $|MA_t|$, opposite to $\theta_{MA,t}$, represents the magnitude of the resultant vector of vectors A_t and M_t (Equation 4).

$$|MA_t| = \sqrt{(a_{x,t}-m_{x,t})^2+(a_{y,t}-m_{y,t})^2+(a_{z,t}-m_{z,t})^2} \quad (4)$$

Therefore, the inclination angle can be calculated as in Equation 5 because it is perpendicular to the angle $\theta_{MA,t}$.

$$I_t = \theta_{MA,t} - 90° \quad (5)$$

It should be noted that the inclination values calculated with this method are only approximate due to the estimation of the gravity vector using the accelerometers. Even with stationary IMUs, vibrations still occur during cycling which introduce error to the magnitude and direction of A_t when attempting to measure g. However, the method used here is sufficiently accurate for the purposes of identifying significant magnetic disturbances, especially since the noise on the A_t signal was found to be approximately Gaussian, with $|A_t|_{mean} \approx 10$ m.s^{-2}.

3.2 KiC data

The KiC algorithm calculates lower limb flexion angles (Figure 6) even in magnetically disturbed environments. In order to compare the KiC data with the Vicon data, it was necessary to ensure that the joint angle definitions were equivalent. For instance, although the knee functional axes are comparable, both hip angle definitions relied on different measurements of pelvic tilt. Therefore, in order for the hip data to be comparative the Vicon pelvic data was used for both data sets to calculate hip flexion. However, there was no known method for aligning the joint axes for the ankle. The sinusoidal flexion curves produced during the repetitive cycling motion were divided into separate pedal revolutions which were then interpolated and averaged to produce a single flexion curve for each joint representative of one pedal revolution during cycling.

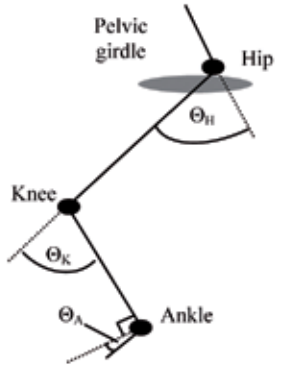

Figure 6: Definition of hip, knee and ankle flexion angles

4. RESULTS

Figure 7 shows the mean intensity readings taken during the MVN recordings by the lower limb segment IMUs for all ten cyclists. The undisturbed magnetic intensity (UI) in the geographical test location was measured at 50 (arbitrary unit) in a calibration test with a MVN IMU. As can be seen from the results, the outdoor environment was almost totally homogenous round the upper leg IMUs, with all mean outdoor values deviating less than 3% from UI. However, the indoor intensity was significantly offset from UI by an 8-10% bias error. Therefore, since this was a trend for all the IMUS during testing, it may be postulated that the indoor magnetic environment was distorted by laboratory-related factors such as ferromagnetic building materials and the indoor trainer used for the laboratory tests. Furthermore, the indoor and outdoor intensities were generally consistent during data collection (average deviations (ADs) were less than 2.5% of UI) as well as between cyclists.

On the other hand, the lower leg (shank) intensities showed a greater divergence between cyclists for both indoor and outdoor tests which suggests that these sensors were more affected by ferromagnetic materials on the bicycles. Moreover, the left shank was the most affected, with both indoor and outdoor intensities significantly higher. The general trend of decreasing homogeneity in the magnetic field, when moving closer to the pedals, was continued in the foot sensor measurements. Some pedal-foot interfaces, such as those for cyclists 5, 6 and 8, severely distorted the field intensity around the foot IMUs. Whereas the upper leg intensities were basically stable, the intensities near the feet varied on average by ~12% in the laboratory and

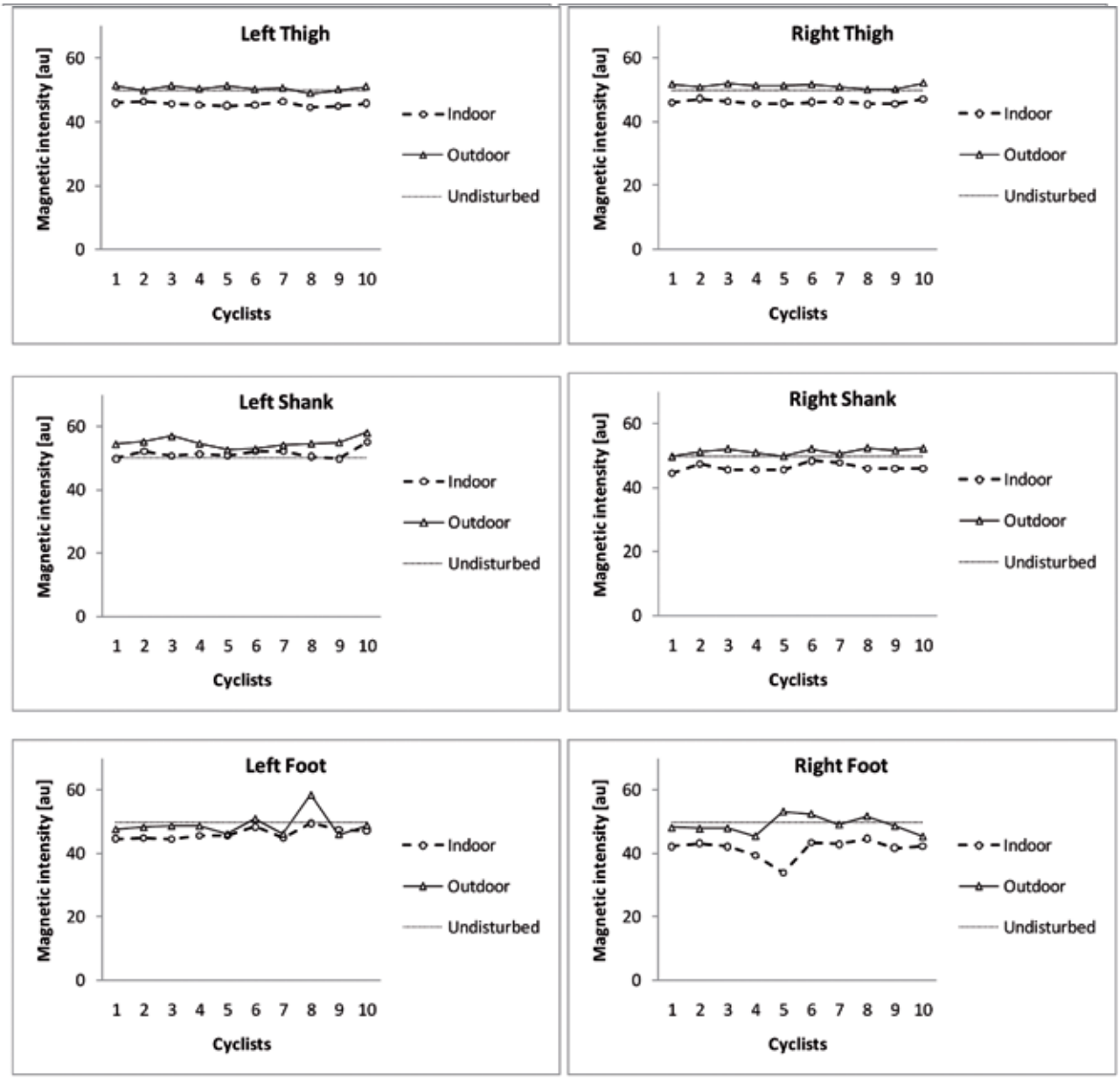

Figure 7: Magnetic field strength measurements for the three sensors on each cyclist's legs

~7% on the road. Some cyclists had disturbances of up to 39% for the left foot sensor.

Figure 8 presents the intensity measurements, as well as the indoor inclination values calculated for the stationary upper body IMUs. Interestingly, except for cyclist 2, results for the pelvic IMU show very little sign of magnetic interference in the seat area for all the cyclists. Similarly, the sternum IMU experienced no significant interference. However, both the sternum and the pelvic IMUs had large variances in their inclination angle values, which were caused by increased noise on the accelerometer signal due to oscillatory pelvic tilt and chest movement due to respiration. Predictably, the magnetic field closer to the handlebars was less homogenous. The left and right forearm sensors were considerably more disturbed than the sternum and upper arms. Even more so, the hands show highly erratic readings for both inclination angle and field strength.

The results from the KiC benchmark test are shown in Figure 9. The correlations between the MVN and Vicon measurements were high for all three joints (Table 1). The Θ_H values ($R^2 > 0.996$) were especially alike, with the root-mean-square error (RMSE) being smaller than 1° for both left and right hips. This is followed by Θ_K ($R^2 > 0.993$), which was still very similar to the Vicon. However, due to diverging measurements near maximum and minimum flexion the RMSEs were 3.4° and 3.1° for left and right legs respectively.

The correlations between measurements for Θ_A were slightly less high ($R^2 > 0.956$). The main reason for this was a significant offset of approximately 8° for the right ankle. The dashed black line represents the ankle flexion

after adjustment for the bias error. The flexion curves for Θ_A appear to have a very similar shape, especially during maximum dorsiflexion (Θ_{MIN}) at the beginning and end of the pedal stroke. However, as Θ_A increases into plantarflexion midway through the pedal stroke the Vicon curve is lower.

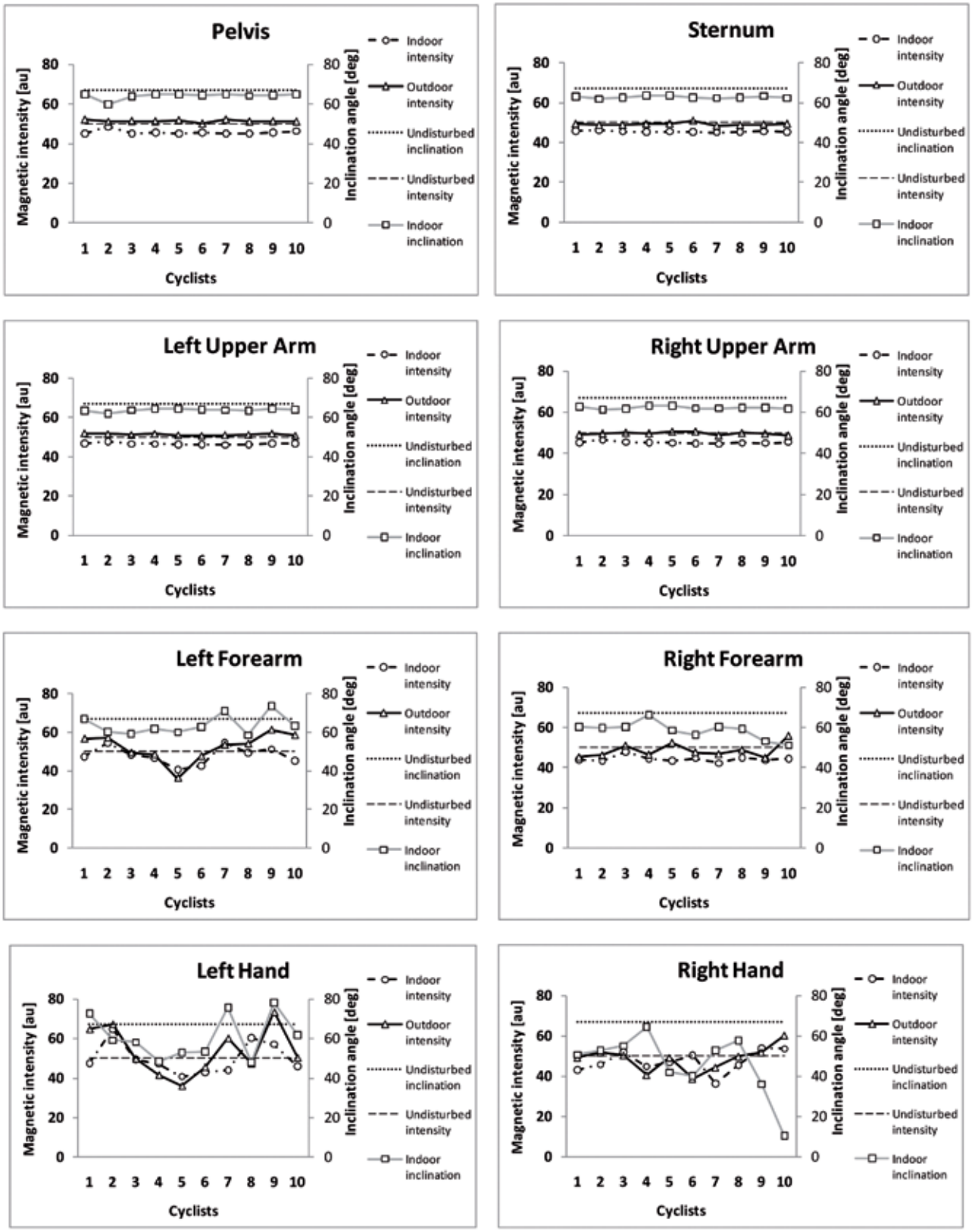

Figure 8: Magnetic field strength measurements for the pelvis, sternum, arm and hand segments

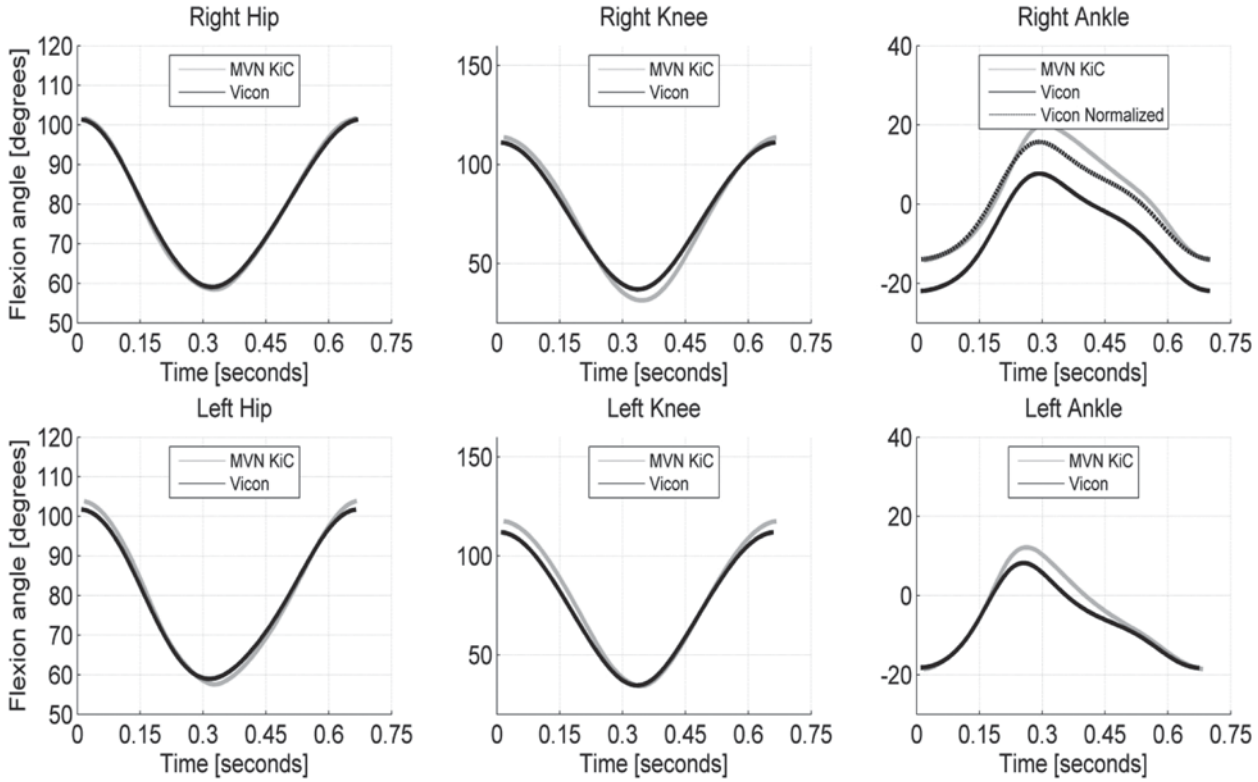

Figure 9: Comparison of right and left leg flexion measurements with Vicon and MVN KiC

Table 1: Benchmark test correlations and RMSE

	R^2	RMSE [°]
Hip [Left/Right]	0.996 / 0.997	0.9 / 0.8
Knee [Left/Right]	0.998 / 0.993	3.4 / 3.1
Ankle [Left/Right]	0.956 / 0.991	2.8 / 2.2

5. DISCUSSION

The interference to the magnetometer readings during the testing reduced the MVN Kalman filter's ability to compensate for gyroscopic drift error using sensor fusion. The resulting instability in the horizontal plane led to varied levels of degradation to the MVN biomechanical model. This was initially observed visually for the lower body in MVN Studio as an exaggerated hip abduction/adduction (due to drifting of the lower leg segment in the horizontal plane relative to the upper leg segment) and unrealistic ankle inversion/aversion (due to drifting of the foot segment relative to the lower leg segment). The disturbances to the arm sensors generally resulted in high uncertainties in the position of the shoulder joint centre and therefore also in the position of the hands segments and elbow and wrist joint angles.

The results of the magnetic analysis showed that the magnetometer measurements of many of the IMUs on the body segments furthest from the bicycle frame were not distorted. However, significant interference was evident in the data from the magnetometers near the handlebars and pedals (distal limb segments). Magnetic intensity levels deviated from the nominal value by an average of 10-15% for the hands and foot sensors, and as much as 50% in some cases. These disturbances are significant, especially when compared to a similar study done with the MVN IMUs on magnetic interference rejection methods, where a disturbance of more than 10% was considered large [13].

The relatively stable magnetic intensity measurements for the upper leg indicate a low level of bicycle-related interference around the hip area. The more disturbed magnetic fields measured around the tibial segment may be explained by the closer proximity of the lower leg sensors to ferromagnetic components such as the gear cogs, chain and other drivetrain elements. The erratic intensities measured by the foot sensors could again be due to different drivetrain materials, as well as metal screws in the cleats, metal clips in the pedals or (as is most probable) a combination of these factors. Although the sensors on the trunk of the subjects were minimally disturbed, the arm sensors showed increasing interference distally, similar to the leg sensors. This suggests that the pedal-foot and handlebar-hand interfaces were highly

disturbed for almost all cyclists due to ferromagnetic bicycle materials.

However, even though the normal MVN filter algorithm could not correctly measure cycling kinematics, the KiC algorithm can still be used to obtain some kinematic parameters despite the disturbances. Although the KiC algorithm performed very well during the validation test, some discrepancies were present between the inertial and optical systems' measurements. For instance, the MVN over-estimates knee extension in the right leg but not in the left. A possible reason for this may be leg length discrepancy, which is taken into account for the Vicon system by separate left and right leg segment measurements whereas the MVN model assumes bilateral symmetry in the biomechanical model. Therefore, these errors in segment length could translate into incorrect joint centre calculations and therefore 'false' or masked differences in left and right flexion. This is definitely a limitation when performing clinical measurements with the MVN, since there is no way to compensate for bilateral asymmetry in the test subject's anthropometry.

However, the difference for the ankle (a significant offset of approximately 8° for the right ankle) was definitely not due to asymmetry alone. The cause of this discrepancy is not known. However, the MVN data is assumed to be incorrect since the Vicon measured left and right ankles in the same region. It is highly likely that some form of experimental error occurred during marker placement. The similarity in the general shape of the curves suggests that the differences in ankle measurements with the Vicon, unlike the offset error for the right ankle, are related to differences in the processing of data for the biomechanical model for the two systems and not experimental error. It appears that the MVN measured ankle plantarflexion slightly high while measuring dorsiflexion very accurately. It is the opinion of the author that the main cause of the problems in the ankle measurement is that the rotational axes of this joint are defined differently in the MVN model to the Vicon model. However, although caution should be taken when interpreting Θ_A, the RMSE was still below 3° after adjustment for bias which is in fact very low.

6. CONCLUSION

The results of this study show that although professional road bicycles consist primarily of carbon-fibre and non-ferrous metals such as aluminium and titanium, they do in fact still cause significant interference to the MVN system when recording road cycling kinematics. Therefore, measurement of full-body kinematics is not yet possible for cycling with IMSs. However, the KiC algorithm does provide measurements of hip, knee and ankle flexion, which are important aspects in the analysis of road cycling technique and bicycle fitting, in hostile magnetic environments. Future work includes more rigorous testing of the KiC algorithm outdoors, as well as developing novel methods of filtering to remove the effect of the magnetic interference during outdoor road testing, with the aim of performing full-body outdoor assessment of cycling biomechanics.

7. REFERENCES

[1] Mündermann, L., Corazza, S. and Andriacchi, T.P. "The evolution of methods for the capture of human movement leading to markerless motion capture for biomechanical applications", *Journal of NeuroEngineering and Rehabilitation,* Vol. 3, 15 March 2006

[2] Eberhart, H. and Inman, V. "Fundamental studies of human locomotion and other information relating to design of artificial limbs" *Report to the National Research Council of the University of California,* 1947.

[3] Mavrikios, D; Karabatsou, V and Alexopoulos, K, et al. "An approach to human motion analysis and modelling", *International Journal of Industrial Ergonomics*, Vol. 36, pp. 979–989, 2006

[4] Cloete, T. "Benchmarking full-body inertial motion capture for clinical gait analysis". *University of Stellenbosch* : MSc thesis, 2008.

[5] Young, A. D., Ling, M. J., and Arvind, D. K. "Distributed estimation of linear acceleration for improved accuracy in wireless inertial motion capture" In *Information Processing in Sensor Networks, Proceedings of the 9th The International Conference in Sensor Networks* (2010), p. In press.

[6] A. Young, M. Ling, and D. K. Arvind, "Orient-2: A realtime wireless posture tracking system using local orientation estimation" in *Embedded networked sensors, Proceedings of the 4th workshop on ACM*, 2007, pp. 53-57.

[7] Cutti, A., Ferrari, A., Garofalo, P. *et al.* "'Outwalk': a protocol for clinical gait analysis based on inertial and magnetic sensors", *Medical and Biological Engineering and Computing,* Vol. 48, pp.17-25, 2010.

[8] Ferrari, A., Cutti, A., Garofalo, P. "First in vivo assessment of ''Outwalk'': a novel protocol for clinical gait analysis based on inertial and magnetic sensors", *Medical and Biological Engineering and Computing* Vol. 48, pp.1-15 .2010

[9] Roetenberg, D., Luinge, H. and Slycke, P. Xsens "MVN: Full 6DOF Human Motion Tracking Using Miniature Inertial Sensors" *Xsens Homepage.* [Online] 8 April 2009. [Cited: 10 January 2010.] http://www.xsens.com/images/stories/PDF/MVN_white_paper.pdf.

[10] Roetenberg, D. "Inertial and Magnetic Sensing of Human Motion" *Universiteit Twente, Netherlands*. PhD thesis, 2006

[11] Garcia-Lopez, J, et al. "Reference values and improvement of aerodynamic drag in professional cyclists", *Journal of Sports Sciences,* Vol. 3, pp. 277-286, 2008

[12] Garofalo, P. "Development of motion analysis protocols based on inertial sensors", *University of Bologna*, PhD thesis, 2010.

[13] Roetenberg, D., Luinge, H.J. and Baten, C.T. M. and Veltink, P.H. "Compensation of Magnetic Disturbances Improves Inertial and Magnetic Sensing of Human Body Segment Orientation" *IEEE Transactions On Neural Systems And Rehabilitation Engineering,* Vol.13. No. 3, September 2005

THE ELECTRO-THERMAL PROPERTIES OF INTEGRATED CIRCUIT MICROBOLOMETERS

M. du Plessis*, J. Schoeman*, W. Maclean* and C. Schutte**

* *Carl and Emily Fuchs Institute for Microelectronics (CEFIM), Dept. of Electrical, Electronic & Computer Engineering, University of Pretoria, Pretoria 0002, South Africa.*
E-mail: monuko@up.ac.za
** *Denel Aerospace Systems (Detek), P.O. Box 7412, Centurion, 0046, South Africa.*

Abstract: The use of uncooled infrared sensors in thermal imaging is a fast growing market in the fields of security and health. The integration of uncooled or room temperature infrared sensors onto a silicon CMOS chip will facilitate the manufacture of large imaging arrays. At the University of Pretoria we are researching the integration of microbolometer infrared sensors onto CMOS readout electronic circuits using post processing techniques. The microbolometer utilises the change in resistance of a temperature sensitive resistive material, e.g. vanadium oxide or a thin metal film, to measure the amount of infrared radiation falling onto the device and heating the device. The microbolometer structure should be thermally isolated from the bulk silicon to achieve the required sensitivity. In this paper we will describe the device structures, as well as the techniques we used to determine experimentally the electrical, thermal and electro-thermal properties of the devices. Of interest to us are the following parameters: 1) temperature coefficient of the bolometer resistive layer, 2) thermal conductivity of the device, 3) thermal capacitance of the total sensor structure and 4) the thermal time constant. The microbolometer thermal characteristics can also be modelled and simulated using CoventorWare software

Key words: Bolometers, infrared imaging.

1. INTRODUCTION

The two principal types of infrared (IR) detectors are 1) photon detectors, and 2) thermal detectors [1]. In photon detectors the absorbed photons produce free electrons and holes in the semiconductor material, to generate a photon-induced current or voltage, either in a photoconductive or photovoltaic mode. Photon detectors have high signal to noise ratios, sensitivity and very fast response, but requires cryogenic cooling systems, which are bulky and expensive. In thermal detectors the absorbed photons produce a temperature change, which can then be detected by measuring a temperature dependent property of the detector material.

Uncooled thermal detectors provide much lower cost, are more compact and dissipate less power. Uncooled IR sensors have been developed in recent years for both military and civilian applications like night vision cameras for surveillance and digital infrared thermal imaging for health applications. Recent advances in micromachining technology allow the fabrication of sensitive thermal detectors that can operate at room temperature and be easily integrated with CMOS readout electronics. This leads to a decrease in power consumption and system cost, which makes hand-held infrared cameras possible. Thermal sensors can be used in two ways [2], namely as 1) direct sensors which convert thermal signals (temperature or heat) into electrical signals, or 2) indirect sensors which are based on thermal actuation effects, for example thermo-mechanical (thermal expansion, bimorph) effects. In this paper we will only consider direct sensors, since it is the most mature technology.

Direct thermal detectors are based on three common approaches [3], namely 1) bolometers, 2) pyroelectric effects, and 3) thermoelectric effects. A bolometer changes its resistance according to the change of the temperature, and thus a high temperature coefficient of resistance (TCR) is needed for high sensitivity. The pyroelectric effect is exhibited by ferroelectric crystals that exhibit electric polarization. The thermoelectric effect takes place when two junctions made of two different materials are at different temperatures, and the magnitude of the voltage generated across the junction (thermopile) depends on the materials and the temperature difference between the junctions. The bolometer type of detector exhibits a much higher responsivity than that of thermopiles, and it is also easier to fabricate than pyroelectric detectors.

The bolometer technology is commercially available in large imaging arrays. In Figure 1(a) the principle of the bolometer detector operation is shown, as well as the conventional thermal model in Figure 1(b).

Infrared radiation falls onto the bolometer device, as shown in Figure 1. The radiation is absorbed by the bolometer device, and if the bolometer is relatively well thermally isolated from the ambient, the temperature of the bolometer will increase. If the bolometer material has a high temperature coefficient of resistance (TCR), the read out circuit can measure the change in resistance and the resistance change will be an indication of the amount of infrared radiation falling onto the bolometer. It is obvious that to achieve a large sensitivity, the bolometer should have a high IR absorption factor, a large TCR and low thermal conductance to the ambient.

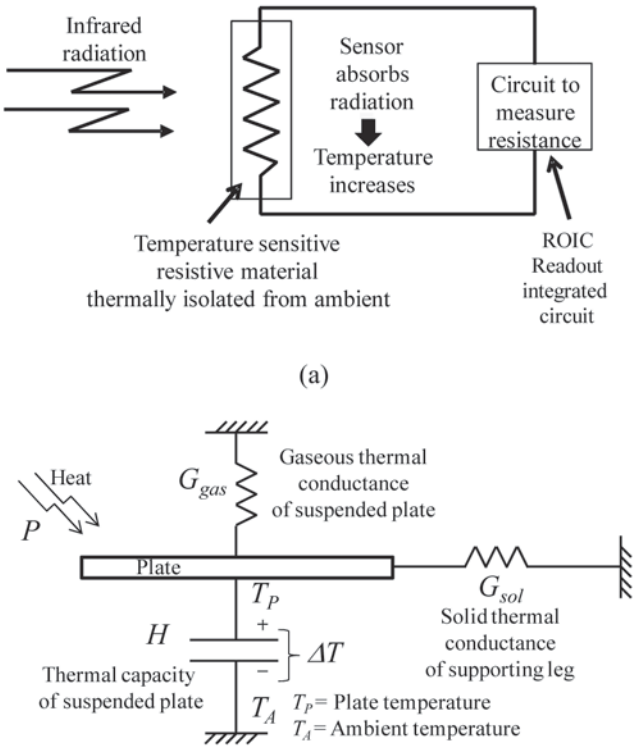

Figure 1: (a) Principle of thermal bolometer sensor, and (b) the equivalent thermal schematic.

2. CONVENTIONAL APPROACH TO DEVICE THERMAL PROPERTIES

The analysis of all types of IR sensors begins with a heat flow equation that describes the temperature rise in terms of absorbed radiant power. There are two potential mechanisms of heat transfer [1], namely 1) thermal conduction, and 2) thermal radiation. Thermal conduction occurs in two ways. Heat flows from the sensor along its mechanical support to the substrate, and heat also flows through the surrounding atmosphere. In practice, the thermal radiation is so small that it can be ignored.

Referring to Figure 1, the rise in temperature ΔT of the bolometer plate is given by [1]

$$\Delta T = \frac{\eta P_O}{G\sqrt{1+4\pi^2 f^2 \tau^2}} \quad ^\circ C \qquad (1)$$

Where:
η = fraction of IR power absorbed
P_O = incident infrared power on detector, W
G = total thermal conductance to substrate, W/K
f = frequency of modulation of radiation, Hz
τ = thermal time constant = H/G, sec
H = thermal capacitance, J/K

If the bolometer is biased with a constant bias current I_B, the voltage responsivity R_V of the bolometer detector is given by

$$R_V = \frac{dV_B}{dP_O} = \frac{dV_B}{dR_B}\frac{dR_B}{dT_B}\frac{dT_B}{dP_O} = \alpha\, I_B\, R_B \frac{\eta}{G} \quad V/W \qquad (2)$$

Where:
I_B = bolometer bias current, A
R_B = bolometer resistance, Ω

$$\alpha = TCR = \frac{1}{R_B}\frac{dR_B}{dT}, \quad \%/K$$

From the above it can be seen that the bolometer voltage signal responsivity R_V is directly proportional to the infrared absorption coefficient η and the bolometer temperature coefficient TCR, and inversely proportional to the thermal conductance G. It is therefore important that the mechanical design of the bolometer support structure must be optimized to minimize thermal conductance G and maximize thermal absorption.

Noise will also be generated within the bolometer imaging system. The noise equivalent temperature difference (NETD in K) is the most important figure of merit used to describe a complete IR imaging system, including the imaging optics. It is defined as the temperature difference on a black object that produces a signal to noise ratio of one at the system output.

$$NETD \propto \frac{v_n G}{A_d \eta \alpha} \qquad (3)$$

Where
v_n = the noise voltage
A_d = the detector area.

The above equation for NETD also shows the relationship between detector area A_d and thermal conductance G to achieve good performance (small NETD). By scaling down to smaller pixel sizes to facilitate the manufacture of larger imaging arrays, the thermal conductance should scale down with detector area. This is difficult, since the length of the connecting legs connecting the thermally isolated microbolometer membrane to the bulk material will determine the thermal conductance in vacuum, needing long legs to achieve a small thermal conductance. The connecting legs can also not take up to much of the pixel area, since the effective fill factor will be reduced.

Knowledge of the thermal properties of the microbolometer membrane is crucial for obtaining optimal performance of the thermal IR detector. The thermal parameter estimations using the conventional approach are discussed below, using Figure 1(b) as reference.

The thermal conductance G of a detector is dominated by the sum of two components [4]:

$$G = G_{gas} + G_{sol} \qquad (4)$$

Where
G_{gas} = conductance through the surrounding gas
G_{sol} = conductance through legs supporting the plate.

The gaseous thermal conductance G_{gas} is given by

$$G_{gas} = \lambda_{gas} \frac{A_d}{d_s} \tag{5}$$

Where
A_d = device area, m^2
d_s = plate to substrate separation, m
λ_{gas} = gas thermal conductivity
= 0.026 W/mK for nitrogen at 1 atm pressure
= 0 in vacuum

$G_{sol} = 2 \times G_{leg}$ when two legs support the plate, with G_{leg} the thermal conductance of one leg. The supporting legs may consist of several layers of different materials. In this case the conductances can be added as a result of parallel conducting paths, and the total leg conductance G_{leg} for one leg will be given by

$$G_{leg} = \sum_i \lambda_i \frac{W_i d_i}{l_i} \tag{6}$$

Where
W_i = width of supporting leg
d_i = thickness of supporting leg
l_i = length of supporting leg
λ_i = thermal conductivity of supporting leg material

It has recently been proposed [5] that the multilayer supporting leg (and suspended plate) can be expressed in terms of an equivalent solid thermal conductivity G_e, with

$$G_e = \lambda_e \frac{W_e d_e}{L_e} = \sum_i \lambda_i \frac{W_i d_i}{l_i} \tag{7}$$

Where
W_e = width of supporting leg
d_e = total thickness of supporting leg
L_e = length of supporting leg
λ_e = equivalent thermal conductivity of supporting leg

And

$$\lambda_e = \frac{1}{W_e d_e} \sum_i \lambda_i W_i d_i \tag{8}$$

The multilayer supporting leg structure of the bolometer can now be represented as a single homogenous structure. The same can be done for the suspended plate region. Under vacuum conditions, the leg conductance will be the dominant thermal conductance, while under atmospheric pressure conditions the gaseous heat transfer will dominate.

In general the heat capacity H is given by

$$H = V \rho c \qquad J/K \tag{9}$$

Where
V = volume of the detector plate, cm^3
ρ = the density of the plate material, g/cm^3
c = the specific heat of the plate material, J/gK

Also, the heat capacity H must be chosen to meet the thermal time constant τ requirement, with

$$\tau = \frac{H}{G} \tag{10}$$

Normally two-dimensional staring arrays are used in bolometer imaging applications. A good choice is to make the pixel time response (equal to the bolometer thermal time constant τ) approximately a third of the frame time (= 1/frame rate). This usually means a thermal time constant τ in the range of 10 ms is required.

3. DEVICE STRUCTURE

Thermal sensors based on CMOS technology became feasible when CMOS micromachining was established. Micromachining makes it possible to remove thermally conducting material for the thermal isolation of heated microstructures. While thermal effects are intuitively considered to be slow, the small size of CMOS microsensors brings about time constants in the millisecond range. Thermally based sensors can be made by combining the well-established industrial CMOS technology with additional compatible processing steps. In our case, the additional compatible processing steps (deposition, lithography and etching) was performed as post-processing, where the additional steps are performed after the completion of the regular IC process sequence.

A typical device we designed and manufactured using one of the CMOS aluminium layers as sacrificial layer, is shown in Figure 2. The bolometer thin film resistance layer was a 60 nm thick and 5 µm wide Ti layer sandwiched in an oxide-nitride membrane structure. The cavity dimension was designed to be 2 micron. The two layout dimensions to be investigated are shown in Figure 3, with Figures 3(b) and 3(c) photomicrographs just after the membrane definition photolithographic step and before the aluminium sacrificial layer etching during manufacture. One would expect FA1 to have the higher thermal conductance at atmospheric pressure because of the larger membrane area, but FA1 should at the same time have the lower thermal conductance under vacuum conditions due to the longer connecting legs, compared to device FA2.

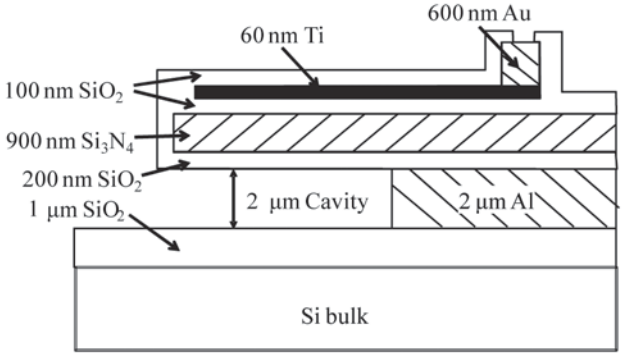

Figure 2: Cross section of bolometer structure.

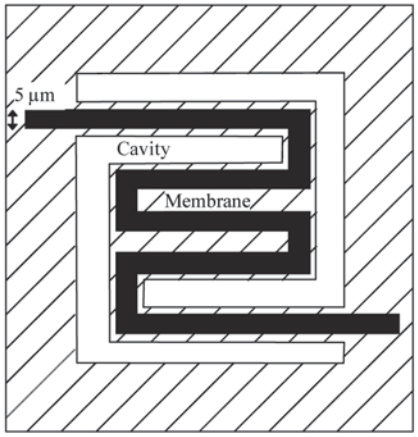

(a)

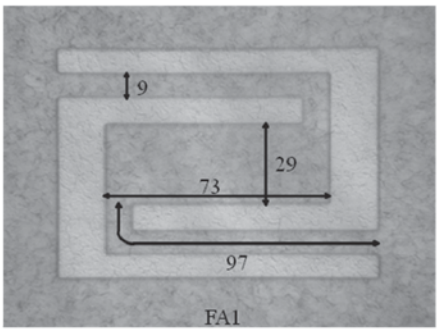

(b)

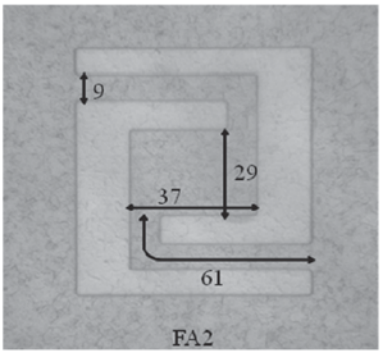

(c)

Figure 3: (a) Titanium bolometer layout and dimensions, (b) device FA1 membrane geometry, and (c) device FA2 membrane geometry.

4. NEW APPROACH TO DEVICE ANALYTICAL THERMAL MODELLING

In this paper we propose a modified approach to the analytical description of metal thin film bolometer thermal properties. The conventional approach described in section 2 and in Figure 1(b) is widely used for all types of bolometers, although it is better suited for devices where the power is dissipated only on the suspended plate, like in the case of high resistance vanadium oxide bolometers, and not within the supporting legs as well. In metal film bolometers power is being dissipated uniformly along the length of the resistor on both the suspended plate and supporting legs.

Four modifications are proposed, namely 1) the effect of sidewall gaseous conduction, 2) a characteristic thermal length constant L_{th}, 3) a distributed thermal resistance network in the bolometer, and 4) a constriction thermal resistance R_C where the supporting leg connects to the suspended the plate.

4.1 Sidewall thermal conduction

The first modification is to include the sidewall heat conduction in the atmospheric pressure analysis. The gaseous thermal conduction is illustrated in Figure 4. As the supporting leg and plate dimensions are shrunk, the sidewall effect will become more pronounced. The sidewall conduction will have the effect of increasing the effective area A_d used in the calculation of the gaseous thermal conductance.

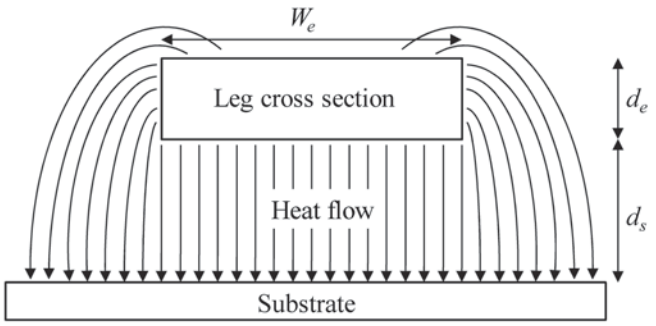

Figure 4: Sidewall thermal conduction model for atmospheric pressure condition.

In our model the effect of the sidewall conduction will be to add a conductance in parallel to the conventional vertical heat flow. Assuming an effective conducting distance d_s+d_e from the sidewall to the substrate, in case of the supporting legs the effective area $A_d = W_e L_e$ will be increased by a factor F_{swl}, with

$$F_{swl} = 1 + \frac{d_s}{W_e}\frac{2d_e}{d_s + d_e} = 1.18 \tag{11}$$

The above value of factor F_{swl} will be the same for both devices FA1 and FA2.

In the case of the suspended plate with lateral dimensions $W_p \times L_p$, the effective area will be increased by the factor F_{swp}, with

$$F_{swp} = 1 + \frac{d_s}{W_p L_p}\frac{2(W_p + L_p - W_e)d_e}{d_s + d_e} \tag{12}$$

The plate factor F_{swp} =1.10 for device FA1 and F_{swp} =1.13 for device FA2.

4.2 Characteristic thermal length

The effect of a characteristic thermal length constant is illustrated in Figure 5. In this figure is shown heat flow P entering one side of the supporting leg, and the resultant

variation in temperature *T(x)* along the leg. The per unit length thermal resistance and conductance in the distributed model are r_{sol} and g_{gas}.

$$r_{sol} = \frac{1}{\lambda_e W_e d_e} \quad , \quad g_{gas} = \frac{\lambda_{gas} W_e}{d_s} \tag{13}$$

The temperature *T(x)* at any position *x* is simply the temperature *T(0)* times an exponential factor.

$$T(x) = T(0)\, e^{-x/L_{th}} \tag{14}$$

with characteristic length

$$L_{th} = \sqrt{\frac{1}{r_{sol} g_{gas}}} = \sqrt{\frac{\lambda_e}{\lambda_{gas}} d_e d_s} \tag{15}$$

4.3 Distributed thermal resistance

The next case to be viewed is the situation in vacuum where heat is generated along the length of a bolometer section. This is illustrated in Figure 6.

In Figure 6 is shown the length *L* of the section, with heat flow *p* into each section of length *Δx*. At the end of the section heat P_E flows into the section from an adjacent section. From Figure 6 the parabolic expression for temperature variation *ΔT(x)* can be derived.

$$\Delta T(x) = \frac{1}{G_{sol} L}\left[(P_S + P_E)x - P_S \frac{x^2}{2L} \right] \tag{16}$$

$$\Delta T(L) = \frac{1}{G_{sol}}\left(P_E + \frac{P_S}{2} \right) \tag{17}$$

Where
G_{sol} = total thermal conductance $= 1/(L \times r_{sol})$,
P_S = total heat flow into section $= \Sigma p$.

4.4 Constriction thermal resistance

Since the microbolometer legs are much narrower than the plate, radial heat conduction is constricted as the heat flows from a wider to narrower cross-section. The analytical model [6] uses a constriction thermal resistance R_C, which accounts for the heat flowing from a wider to a narrower cross-section. The constriction resistance R_C is given by [6]

$$R_C = \frac{1}{\pi d_e \lambda_e}\left[\left(\varepsilon + \frac{1}{\varepsilon} \right) \ln \frac{1+\varepsilon}{1-\varepsilon} + 2 \ln \frac{1-\varepsilon^2}{4\varepsilon} \right] \tag{18}$$

with $\varepsilon = \frac{W_e}{W_p}$ and W_p = width of plate.

In our approximation the constriction resistance will be distributed over the characteristic length L_{th}.

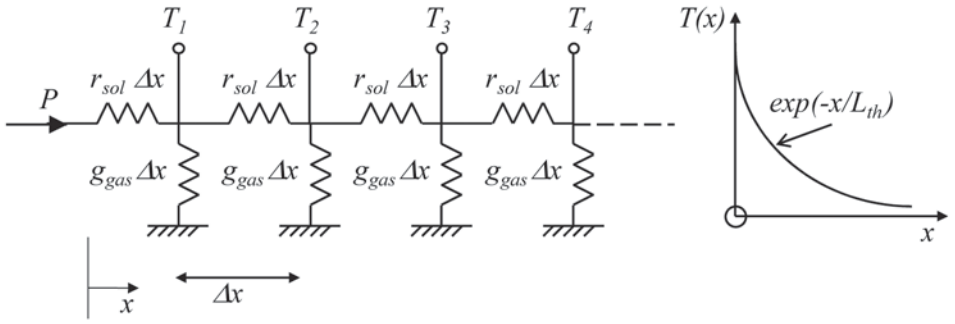

Figure 5: Distributed thermal resistance model for atmospheric pressure condition.

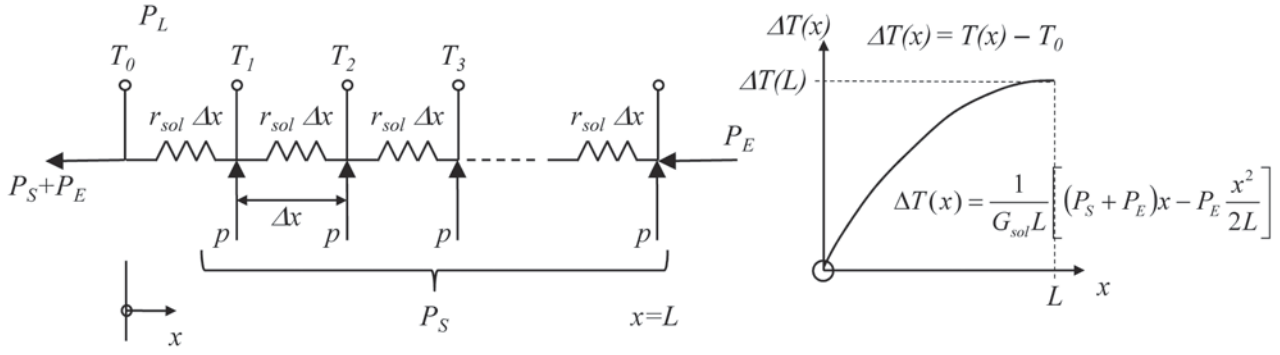

Figure 6: Distributed thermal resistance model for vacuum condition.

Table 1: Thermal constants used in prototype calculations.

Material	Thermal conductivity λ W/mK	Specific heat c J/gK	Density g/cm^3
CVD Silicon dioxide	0.76	1	2.22
CVD Silicon nitride	1.65	1.2	3.10
Titanium	16.3	0.5	4.51

Table 2: Thermal parameters used in prototype calculations.

Test device	Width W_e µm	Thickness d_e µm	Conductivity λ_e W/mK	Length L_{th} µm	Width W_p µm	Resistance R_C mK/W
FA1	9	1.36	1.71	13.4	73	469×10^3
FA2	9	1.36	1.71	13.4	37	287×10^3

5. ANALYTICAL MODELLING AND COVENTORWARE SIMULATION

The thermal properties of the two test devices were calculated from the device dimensions in Figures 2 and 3, analytical expressions of section 2 and 4, and the thermal constants and parameters listed in Tables 1 and 2.

Using the above values and analytical expressions, the temperature profiles in the test devices could be estimated. The test devices were also simulated using commercial CoventorWare software.

In Figure 7 is shown the one dimensional temperature profile along the supporting leg from the substrate to the centre of the plate, for device FA1, under atmospheric pressure conditions. The three temperature profiles are: 1) the conventional analysis, 2) the modified analysis, and 3) the CoventorWare simulated results.

In Figure 8 are shown similar results for the FA1 test device under vacuum conditions. In this case both the modified model and conventional model are fairly close to the simulated CoventorWare values.

The average temperature along the length of the metal film resistor can be determined from Figures 7 and 8, and with the known input thermal power, the theoretical thermal conductance for each device can be determined at atmospheric pressure and under vacuum conditions.

From Figure 7 it is evident that the inclusion of the sidewall effect F_{sw}, the characteristic thermal length L_{th} and the constriction resistance R_C, greatly improved the accuracy of the analytical modelling of the device. The fact that the CoventorWare simulation result has a slightly lower average temperature than the modified analytical model indicates that the sidewall effect may be slightly underestimated in our model. This lower average temperature of the CoventorWare simulation may, however, also be due to the gradual increase in temperature with distance where the supporting leg connects with the substrate (x = 0) which we do not model analytically. It was furthermore interesting to note in the 3-D Coventorware simulation results that the sidewall effect of gaseous conduction could be observed in the atmospheric pressure case, since the edges of the plate were cooler than the rest of the plate.

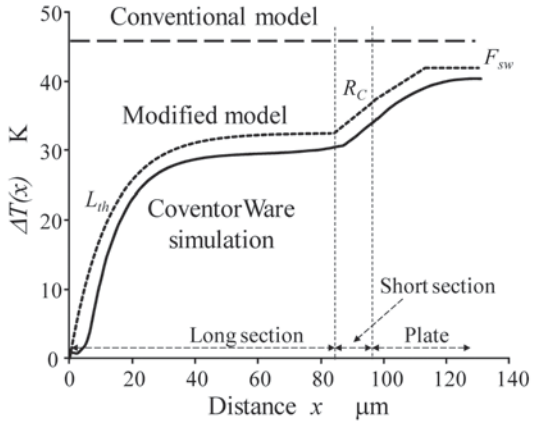

Figure 7: Thermal profiles at atmospheric pressure for bolometer device FA1.

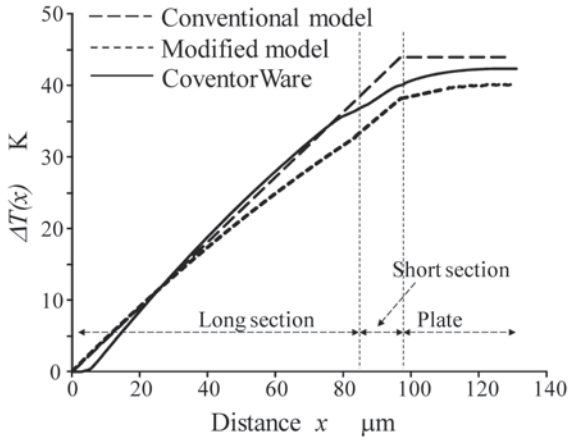

Figure 8: Thermal profiles under vacuum conditions for bolometer device FA1.

6. PARAMETER EXTRACTION

A thin film metal resistor value as a result of a temperature increase can be modelled as

$$R_B(\overline{\Delta T}) = R_O(1+\alpha \times \overline{\Delta T}) \tag{19}$$

with $\overline{\Delta T}$ = the average temperature along the length of the resistor. In our devices the temperature will not be constant along the length of the thin film resistor. The TCR of the Ti metal layer was experimentally determined as α = 0.1 %/K, following the above linear relationship closely.

By passing a bias current I_B through the bolometer, and measuring the bolometer resistance R_B as a function of bias current, the thermal conductance can be determined. Using the above equation of resistance as a function of temperature change, as well as the fact that

$$\overline{\Delta T} = \frac{P}{G} = \frac{I_B^2 R_B}{G} \qquad ^\circ C \tag{20}$$

it can be shown that

$$\frac{1}{R_B} = \frac{1}{R_{BO}} - \frac{\alpha I_B^2}{G} \tag{21}$$

By plotting the inverse of the bolometer resistance as a function of the bolometer bias current squared, the thermal conductance G can be determined from the slope of the graph. The experimental results for FA1 and FA2 under atmospheric pressure are given in Figure 9. Unfortunately test devices packaged in a vacuum less than 0.1 mbar are not yet available.

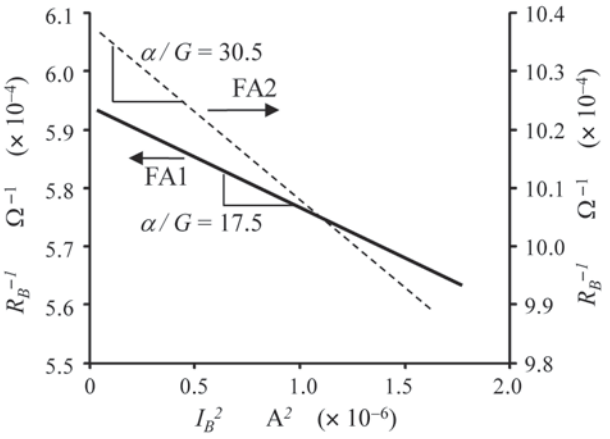

Figure 9: Experimental determination of thermal conductance at atmospheric pressure.

With the known values of the TCR (α), the experimental thermal conductance under atmospheric pressure can be determined from Figure 9.

The experimental values and the simulated values using CoventorWare under atmospheric pressure conditions are listed in Table 3.

Table 3: Simulated and experimental thermal conductances.

	Atmospheric pressure		Vacuum
	CoventorWare G μW/K	Experiment G μW/K	CoventorWare G μW/K
FA1	72.4	59.4	0.6
FA2	44.7	34.1	1.2

In general the experimental values are about 20% smaller than the simulated values. Since the gaseous thermal conductance at atmospheric pressure scales linearly with detector area and inversely with the plate to substrate cavity spacing d_s, the difference between the simulated and experimental thermal conductance may be as a result of variations in cavity separation due to stresses in the suspended plate and supporting legs. The simulated values were simulated with the theoretical value of d_s = 2 μm, while the experimental devices may have a slightly larger cavity dimension.

To experimentally determine the thermal capacitance H and thermal time constant τ, a transient measurement was performed. In this measurement the bolometer bias current i_B is switched between two values, I_L and I_H as shown in Figure 10.

The bolometer steady state output voltage will change from V_L to V_H with $R_H > R_L$ the two steady state bolometer resistances. The transient behaviour between the two steady state values will be determined by the thermal transient characteristics of the bolometer. A typical result is shown in Figure 11 for device FA1 under atmospheric pressure conditions.

From the transient, the thermal time constant τ can be determined. The experimental time constant τ under atmospheric pressure for the test devices are shown in Table 4, as well as the derived thermal capacitance H for each device. The atmospheric pressure thermal conductance and thermal capacity both scale linearly with the detector area and one would expect the two test devices to have the same atmospheric pressure thermal time constant.

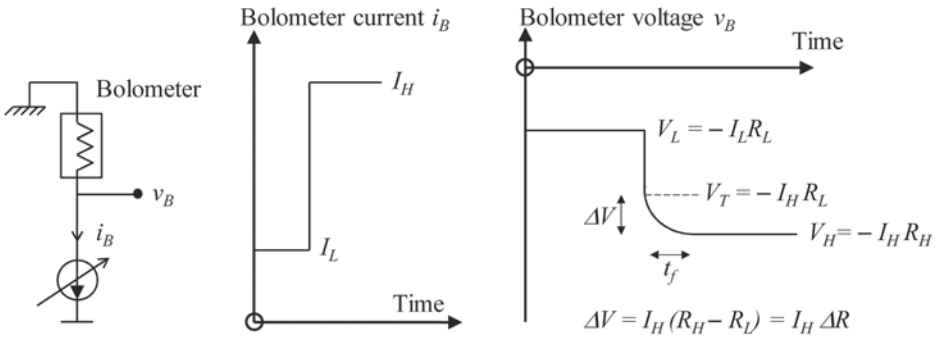

Figure 10: Transient switching behaviour of bolometer test circuit.

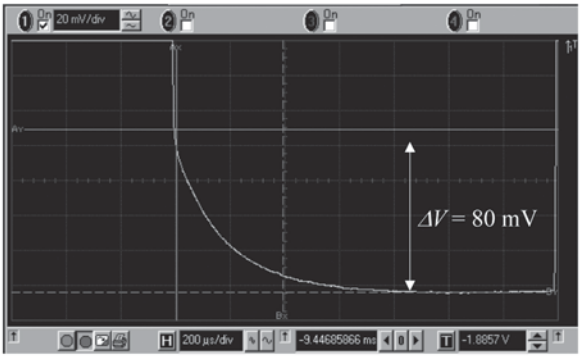

(a)

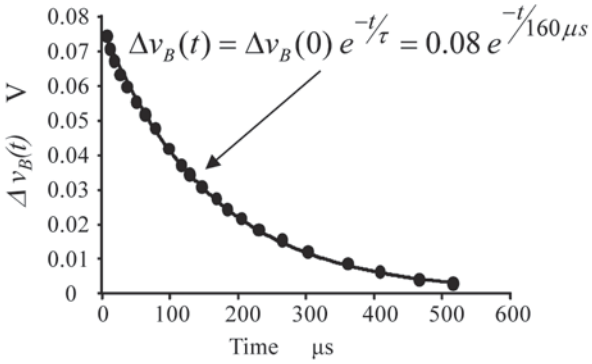

(b)

Figure 11: (a) Experimental switching transient, and (b) exponential time constant fit for FA1.

Table 4: Experimental atmospheric pressure thermal time constant and thermal capacity.

Device	Thermal time constant τ	Thermal capacity H
FA1	160 µs	9.5 nJ/K
FA2	164 µs	5.6 nJ/K

7. CONCLUSIONS

A modified theoretical model has been proposed for microbolometers. It was shown that this model approximates the CoventorWare simulation quite well, especially for devices under atmospheric pressure. Extracted experimental values of the thermal parameters were compared to the theoretical values and differences explained.

It was found that the three modifications we proposed, for atmospheric pressure conditions, namely 1) the effect of sidewall gaseous conduction, 2) a characteristic thermal length constant L_{th}, and 3) a constriction thermal resistance R_C where the supporting leg connects to the suspended the plate, significantly improved the accuracy of the analytical modelling of the bolometer devices.

It was also found that under vacuum conditions the conventional analytical models are adequate.

8. ACKNOWLEDGEMENT

This project was financially sponsored by the AMTS (Advanced Manufacturing Technology Strategy), a strategy of the Department of Science and Technology.

9. REFERENCES

[1] P.W. Kruse and D.D. Skatrud (Editors): *Uncooled infrared imaging arrays and systems*", Academic Press, London, Semiconductors and Semimetals, Volume 47, 1997.

[2] H. Baltes, O. Paul and O. Brand: "Micromachined thermally based CMOS microsensors", *Proceedings of the IEEE*, Vol. 86, No. 8, pp. 1660-1676, August 1998.

[3] A. Rogalski: "Optical detectors for focal plane arrays", *Opto-Electronics Review*, Vol. 12, No. 2, pp. 221-245, 2004.

[4] P. Eriksson, J.Y. Andersson and G. Stemme: "Thermal characterization of surface-micromachined silicon nitride membranes for thermal infrared detectors", *Journal of Microelectromechanical Systems*, Vol. 6, No. 1, pp. 55-61, March 1997.

[5] N. Topaloglu, P.M. Nieva, M. Yavuz and J.P. Huissoon: "A novel method for estimating the thermal conductance of uncooled microbolometer pixels", *Proceedings of the IEEE International Symposium on Industrial Electronics ISIE 2007*, Vigo, Spain, pp. 1554-1558, 4-7 June 2007.

[6] N. Topaloglu, P.M. Nieva, M. Yavuz and J.P. Huissoon: "Modeling of thermal conductance in an uncooled microbolometer pixel", *Sensors and Actuators A*, Vol. 157, pp. 235-245, February 2010

INVESTIGATION INTO A MULTILATERATION LASER TRACKING SYSTEM FOR THE NATIONAL METROLOGY INSTITUTE OF SOUTH AFRICA

G.P. Greeff* and O.A. Kruger **

* National Metrology Institute of South Africa, Dimensional Laboratory, Private Bag X34, Lynnwood Ridge, Pretoria 0040, South Africa. E-mail: *pgreeff@nmisa.org*
** National Metrology Institute of South Africa, Dimensional Laboratory, Private Bag X34, Lynnwood Ridge, Pretoria 0040, South Africa. E-mail: *oakruger@nmisa.org*

Abstract: A baseline study for the implementation of multilateration with a laser tracker for the Dimensional Laboratory of the NMISA (National Metrology Institute of South Africa) was completed. Software which requires one laser tracker to perform sequential multilateration was developed for the lab. Simulation studies are also done with this program for verification and configuration motivation purposes. Other aspects of the study involved developing a prototype laser tracker station and performing kinematic simulation analysis on gimbal type trackers. With practical experience gained, recommendations are made for future multilateration development in the Dimensional Laboratory.

Keywords: Multilateration Laser Tracker, Three Dimensional Coordinate Measurement, Dimensional Metrology

1. INTRODUCTION

The NMISA (National Metrology Institute of South Africa) is responsible for development, dissemination and maintenance of the national standards. The Dimensional Laboratory of the NMISA is responsible for maintaining the national standard of length, an iodine stabilised He-Ne laser. Part of the responsibilities of this group is to provide traceability from this national standard for three dimensional measurement systems.

Fast and accurate three dimensional measurements are critically to the manufacturing industry. Various instruments are used to measure individual parts as well as the alignment during the assembly processes of large scale projects. Measurements are required from projects such as ship building and aeroplane construction, to smaller products such as rotor blades, satellite dish antennas, turbines and the motor industry. Basically, any manufactured product needs to be measured dimensionally, at some stage, for assembly or quality assurance purposes. Measurement instruments used include photogrammetry systems, bridge type CMMs (Coordinate Measuring Machine), portable measurement arms, total stations, indoor GPS systems and laser trackers [1].

Currently commercial laser trackers, utilizing interferometric laser distance measurements and angular encoders, remain one of the most versatile and accurate three dimensional measurement systems. This accuracy can be further improved by using a technique called multilateration, where only the distance component of multiple trackers is used to calculate the target point coordinates. A multilateration system is therefore directly traceable to the metre, reducing uncertainties caused by intermediate calibration steps, and eliminating the less accurate angle measurements [2].

Note that a technique where only one tracker is used to perform multilateration is called sequential multilateration. This technique is more feasible to implement, given the cost of laser trackers [3]. The repeatability of the target points will however affect the obtainable absolute accuracy.

The level of the required accuracy of dimensional metrology in manufacturing industries is increasing and this is the main motivation for the project; i.e. the need for more accurate coordinate metrology for the NMISA. This article will briefly explain how a tracker works, report on a prototype built and describe the concept of multilateration, as well as report on results of the project. The article starts with commercial laser trackers, as the building block for a multilateration system, which either uses more than one tracker, multilateration, or one tracker positioned at different locations, sequential multilateration. The main focus however of the project is to investigate the concept of multilateration for the purpose of practical laboratory implementation.

2. THE LASER TRACKER WORKING PRINCIPLE

The concept of the current commercial laser tracker, patented by [4], consist of the following main components: a laser source, a beam steering mechanism with angle encoders, an interferometer block, an optical sensor called a Position Sensitive Diode (PSD), beam splitting optics, a retroreflector, a control unit and software. These components are used to both track the target and measure the coordinates of the target (see Figure 1).

The source beam is split with a beamsplitter into a measurement and reference beam. The measurement beam travels from this beamsplitter to the target (the retroreflector) and back. After returning from the target it will interfere with the reference beam and this

interference will be used to determine the relative change in distance to the target.

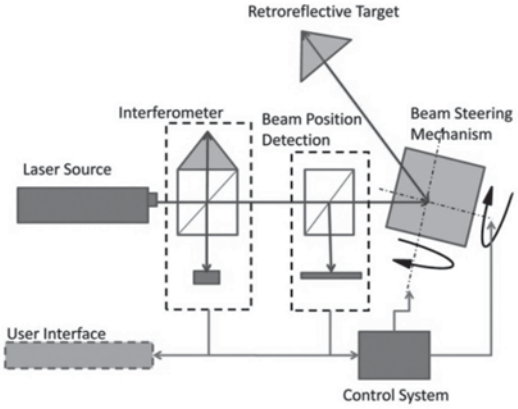

Figure 1: Schematic of Laser Tracker Components (Based on [4])

The measurement beam is steered towards the target with a mirror mounted on the beam steering mechanism. If the returning measurement beam does not return sufficiently onto the reference beam the interferometer will loose its reference and not be able to determine the change in distance to the target. The target therefore needs to be tracked, by minimizing the measured displacement between the outgoing and returning measurement beam (see Figure 2).

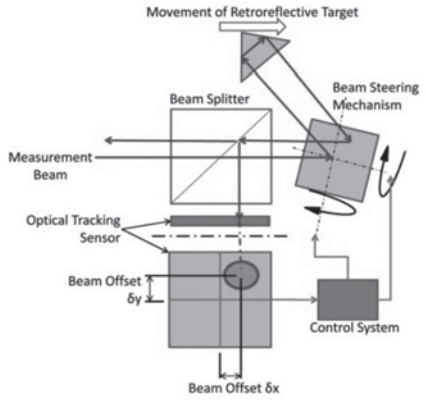

Figure 2: Schematic of Tracking Operation

This displacement is detected with the PSD. The optical sensor has four electrodes, each of them producing an amount of photo-current relative to the distance of the electrode to the centre of the beam spot. These photocurrents are amplified and converted to four voltages, which are used to determine the position of the centre of the beam on the sensor's active area [5]. The controller uses the detected offsets to minimize the tracking error by rotating the beam steering mirror to re-centre the beam on the PSD.

Note that an ADM (Absolute Distance Measurement) system does not need to track a target, while a distance interferometer system does. However current commercial interferometer systems are more accurate than current commercial ADM systems. The interferometer measurement is only a relative distance, not an absolute one. This affects a tracker in two ways: (1) an initial offset distance is needed and (2) that the target must be tracked at all times. There are commercial systems which combine both ADM and interferometer systems, mainly to enhance the speed and ease of measurements. Work however is being done to improve ADM accuracy to achieve sub-fringe resolution [6]. If ADM technology replaces the relative interferometric system, the target would not need to be continuously tracked any longer.

The three dimensional coordinates of the target is determined with two angles and one radius: the two encoder readings and the interferometric length measurement plus an initial offset distance.

This offset distance is relative to a home position. It is ideally equal to the difference between the distance from the measurement beam incident point on the beam steering mirror to the target point and from the same incidence point to the home position.

3. LASER TRACKER PROTOTYPE

A prototype laser tracker was designed and built to evaluate the feasibility of building a precision laser tracker for multilateration purposes. As well as to better understand the engineering challenges, scope and design parameters involved in such a project. The focus was specifically on the tracking sub-system (Figure 2), since the distance interferometric sub-system is well understood and easily implemented as a modular unit.

The prototype design involved (1) designing and building a beam steering mechanism, (2) sensor signal conditioning and (3) control of the system. For this project a single mirror gimbal was selected (Figure 3) for the beam steering mechanism, as it was the least complicated mechanism.

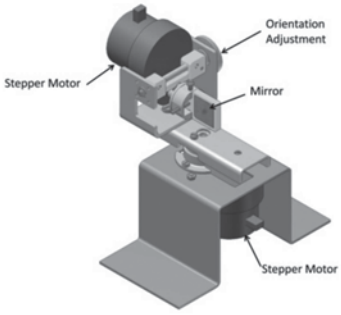

Figure 3: Drawing of the Prototype Tracker

An amplifier circuit, consisting of a current to voltage converter and amplification unit, was designed for the signal conditioning and for control of the system a microcontroller (dsPIC30f4011 from Microchip) was used. The microcontroller receives commands from a GUI (Graphical User Interface) on a PC via a RS232 connection. It also converts the sensor signals from the amplifier with an ADC (Analogue to Digital Converter),

from which it determines the required commands to actuate the beam steering mechanism.

Four concepts are found in literature for the beam steering mechanism: gimbal [4], hemi-spherical [7], two mirrors [5] and spherical [8]. The gimbal is a single mirror (see Figure 3) beam steering concept. The hemi-spherical concept places the mirror on the flat of a hemi-sphere, and the two mirror concept uses a separate mirror for each axis of rotation. The spherical concept rotates the interferometer block around a reflective sphere.

A gimbal type beam steering mechanism was selected and is actuated with two geared stepper motors, driven with PWM (Pulse Width Modulated) signals via an H-bridge. The steppers are micro-stepped, to make the step resolution finer, by providing it with a micro-stepping sequence. A single beam laser tracking system consists of different components and interfaces. If this is joined with optical design and laser requirements, it becomes clear that such a system is a unique optical, mechanical and electronic engineering design challenge.

3.1 Laser Tracker Prototype Tests

Tests were performed with the prototype, to investigate the tracker's tracking ability. It was found that the system can track a target moving in a volume of 200x200x200 mm^3, at a distance of 300 mm from the tracker. It was decided that this is sufficient evidence for the working of the prototype station.

Table 1: New Specifications (Based on [9])

Parameter	Prototype	Ideal Specification
Angular Resolution	0,06 - 0,004 °/step* (1047 - 70 µrad)	0,0006 °/step (10 µrad)
Angular Speed	Not measured	10 m/s
Angular Acceleration	Not measured	19 m/s^2

*Minimum theoretically, with 16 bit microstep resolution

Testing of the prototype showed that fast direction change, very small step size and accurate positioning are the critical parameters for the beam steering mechanism. Table 1 quantifies the ideal specifications, based on existing system specification found in literature. A backlash free actuator will also increase the direction change speed.

3.2 Kinematic Modelling of a Gimbal Type Tracker

The kinematic model of [10], describes a two axis gimbal type laser tracker, ten parameters were used and simulated. This was done to gather a better understanding of a single laser tracker and its error sources. The model only focuses on the measurement error due to the beam steering system and does not account for errors in the retroreflector or the PSD.

The simulations were used to investigate how the measurement is influenced by various factors. Monte Carlo analyses were used to do these investigations. This is done with a set of Target Point (TP) coordinates. The target points formed a regularly spaced array in three-dimensional space and the simulation replicated the measurement of this array with a tracker. Uncertainty or errors were added to the tracker parameters, to investigate the spatial error effect of each parameter individually and combined.

The most significant conclusion of these simulations confirmed another study's results [11] and was that any lack of orthogonality between the rotation axes is a major cause of a shifting centre of rotation. The incidence point and the centre of rotation are consequently not coincident, which creates an error in the interferometric dead path, since the interferometer assumes the distance from the interferometer to the first point remains constant [9].

4. MULTILATERATION

4.1 Multilateration Concept

Multilateration is similar to trilateration (the determination of a target point, if three station points are given, along with the distance from each station point to the target point) with the main difference that the station point locations are not exactly known. However, if there are four station points a redundant equation, in terms of trilateration, will be obtained per target point. If sufficiently accurate initial target and station point coordinates, along with accurate lengths, are given, then the exact point coordinates can be solved (approximated) by a non-linear least square optimiser. The offset interferometric distance is also included as a variable in the optimiser. The optimiser then seeks the best fit for each tracker's offset distance and all the target point coordinates.

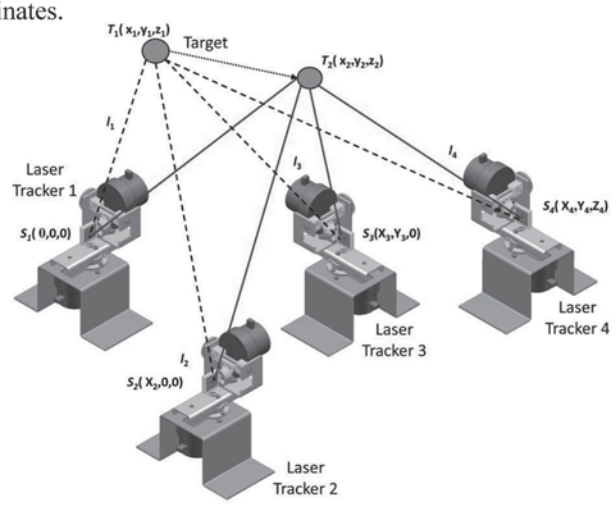

Figure 4: Schematic of a Multilateration Laser Tracking System, with Four Trackers. (Note the assumed initial position of the trackers, to reduce the number of variables)

A MLTS (Multilateration Laser Tracking System) therefore consists of a number of laser trackers (see Figure 4), coupled to software which performs post processing. Some MLTS use purpose built trackers, which do not have angle encoders [8], whilst others use the encoders to improve the measurement, by compensating for the tracking mirror centre rotation errors [12].

A MLTS satisfies the Abbé principle (i.e. the axis of measurement should be inline with axis of displacement to be measured), has direct traceability to the length standard, is self-calibrated with respect to its own position and is therefore superior to the conventional bridge-type CMMs [2,10]. For example, to measure any point the bridge type CMM must measure distances along three axes (X, Y and Z) sequentially, whilst a MLTS achieves this directly, without an Abbé error. The positional self-calibration of a MLTS also creates a virtual metrology frame, making it more portable [8] than a conventional CMM. The measurement range can be extended by only moving one tracker base station at a time. This allows, for example, the measurement of an object from all sides. [13] add that such a system (after self-calibration) can determine the position of the target or the initial distance for a laser tracker, in the event of one of the trackers losing the target. This overcomes the main limitation of an interferometric laser tracker: that the target must be tracked at all times. Self-calibration also negates the requirement for tedious measurement preparations [2].

A disadvantage of such a multilateration system is that the measurement volume is limited, compared to a single beam system [5]. High speed tracking is also vital, which necessitates an advanced control system, as shown by [14]. Furthermore, a laser tracker is an expensive system.

The MLTS software determines the offset distances and coordinates of the targets and tracking stations by using a non-linear least squares optimiser. The least squares algorithm tries to fit all the system variables to all the length measurements. The measurements are defined as the distances from the tracker mirror centre of rotation to the targets. The system variables are defined as the tracker coordinates, the offset (reference) length of each tracker and the target variables.

For n target points and four trackers, there are $3n$ target variables and $4n$ known measurements values. This implies that at least ten target points are required to solve the whole system. The coordinate system can be fixed, without loss of generality, by three assumptions regarding the positions of the tracking stations: the first station is at the origin $(0,0,0)$, the second tracker is only displaced in the X direction $(x,0,0)$ and the third tracker is in the XY plane $(x,y,0)$ [2].

The unknown variables (for n target points and m tracker stations) can be solved, given the required initial (estimated) values for system variables by minimizing the total system cost, or cost function, defined as:

$$E = \sum_{j=0}^{m} \sum_{i=0}^{n} {e_{ij}}^2 \qquad (1)$$

The residual e_{ij} for the j^{th} measurement station and i^{th} target point is [2]:

$$e_{ij} = \sqrt{\left(x_i - X_j\right)^2 + \left(y_i - Y_j\right)^2 + \left(z_i - Z_j\right)^2} - \left(l_{ij} - L_j\right) \qquad (2)$$

with the target coordinates $(x,y,z)_i$, the measurement station coordinates $(X, Y, Z)_j$ and the distance measured (l_{ij}). Note that all the length measurements (l_{ij}) are relative to an initial length (L_j) for each tracker. The length measurements are therefore given by $(L_i + l_{ij})$, where l_{ij} is the actual interferometric length measurement.

For the initial (estimated) values the measurements of the first tracker are used for the target point coordinates. The position of each tracker station relative to the first station is measured and this is used to provide all the initial stations' coordinates.

4.2 *Sequential Multilateration Test*

A Python program was developed at NMISA, based on the concept described above. Given a set of measured lengths and estimated initial positions for the tracker stations and target points, it searches for a possible fit, which minimizes the cost function (1).

Tests were done at NMISA using a commercial laser tracker and a CMM, in the Dimensional Laboratory. A magnetic retroreflective target holder was mounted on the CMM, which was programmed to move to five points (four corners and a middle point) in four vertical planes as shown in Figure 5. The tracker was positioned at 6 different points, around the CMM. The target was tracked and when the CMM came to a halt at a point, a measurement was taken. All 20 target points were measured from each of the 6 locations.

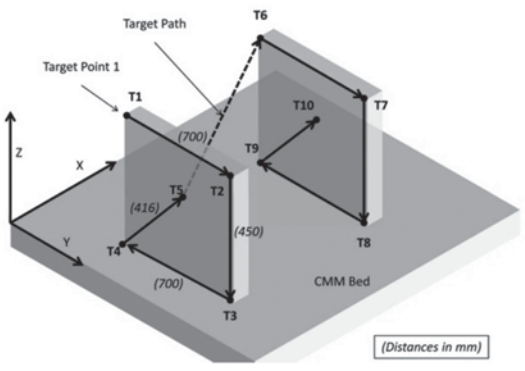

Figure 5: Target Point Array Created by the CMM

A local minimum for the cost function was found by the program for the system variables and measurements. The initial cost of the system was around 3250 mm. This was reduced to 10,054 µm.

The optimiser uses either its own numerical approximation for the Jacobian of cost function, or a user defined analytical matrix. An analytical Jacobian was used and it reduced the number of function call dramatically (300 to 7 iterations). The final cost though stayed the same (at 10,054 µm).

The commercial laser tracker software however does not output the raw interferometric length, only the post-processed absolute coordinates relative to the tracker's home position. The initial length variables were therefore suppressed in the algorithm. Since the same tracker is used for all the measurements, it is assumed to have a negligible effect in the comparison between the individual tracker and the algorithm result.

Table 2: Estimated Maximum Uncertainty

Uncertainty Contributor	Specification (µm, L in m)	Contribution (µm)
CMM	$(2{,}4 + 3L_c)^*$	5,4 (Max L_c: 1 m)
SMR and Tracker Repeatability	10,7	10,7
Tracker:		$7{,}55^{**}$
Radial	$(1 + 1L_r)^*$	(Max L_r: 4 m)
Transverse	$(3 + 1L_t)^*$	(Max L_t: 1 m)

* From manufacturer specification

** $\sqrt{(1+4)^2 + 2(3+1)^2} = 7{,}55$

The accuracy of the system variables, which gives the local minimum, was further investigated using three dimensional distances. Such a distance between TP (Target Point) *i* and *j* is calculated with Pythagoras as:

$$d = \left|TP_i - TP_j\right| \quad (3)$$

All the possible three dimensional distances can be calculated for an array of TP. The resulting array from the optimizer (or fit) can then be compared with the individual tracker measurements and the expected CMM movement. The CMM movement however will not be ideal, but should be within an uncertainty. The fit and measurements can still be compared with the ideal CMM movement and should fall within this uncertainty. From Table 2 the maximum expected error for a point can be calculated by taking the sum of all the contributions, which is 23,7 µm, multiplying this with two, gives an estimate of maximum expected error in the distance between any two points, which is 47,3 µm.

Figure 6 shows the average deviation for four significant distances: the 200 mm X axis, 700 mm Y axis, 450 mm Z axis and 416,083 mm YZ distance. The measurements in the graph fall within the expected range, whilst the fit result falls outside the range for the Z and Y axes distances. This result is useful, since it gives a method to evaluate the accuracy of the fit, apart from the cost function. The cost function therefore is not a sufficient indication for the accuracy of the resulting fit.

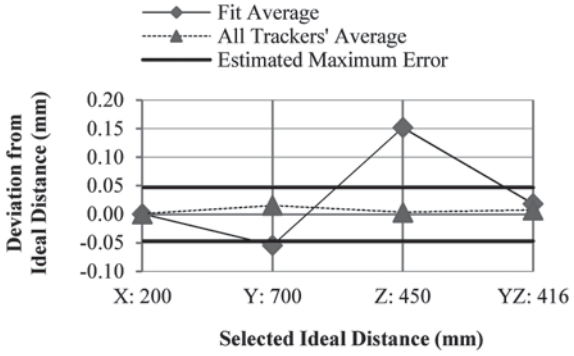

Figure 6: Average Deviation from Ideal CMM Distances (For the fit and the average of all 6 tracker positions).

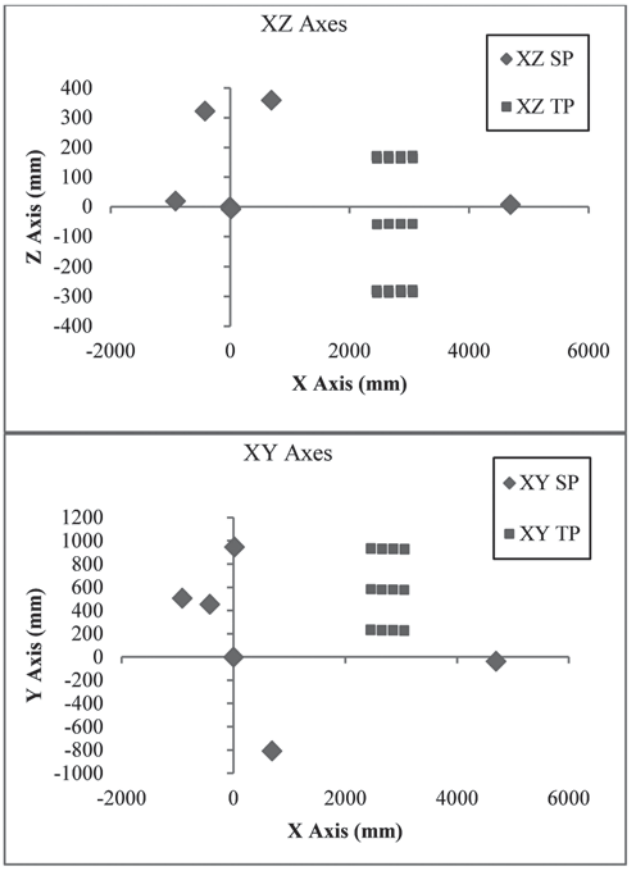

Figure 7: Configuration for Test (SP: (Tracker) Station Point)

4.3 *Improving the Sequential Multilateration Test Configuration*

Unfortunately the tracker used for the test stopped functioning and further tests could not be performed. Simulations however were used to test and improve the algorithm. Figure 6 showed a large deviation in some of

the distances. The cause for these discrepancies is thought to be the configuration of the tracker stations around the TP array (see Figure 7).

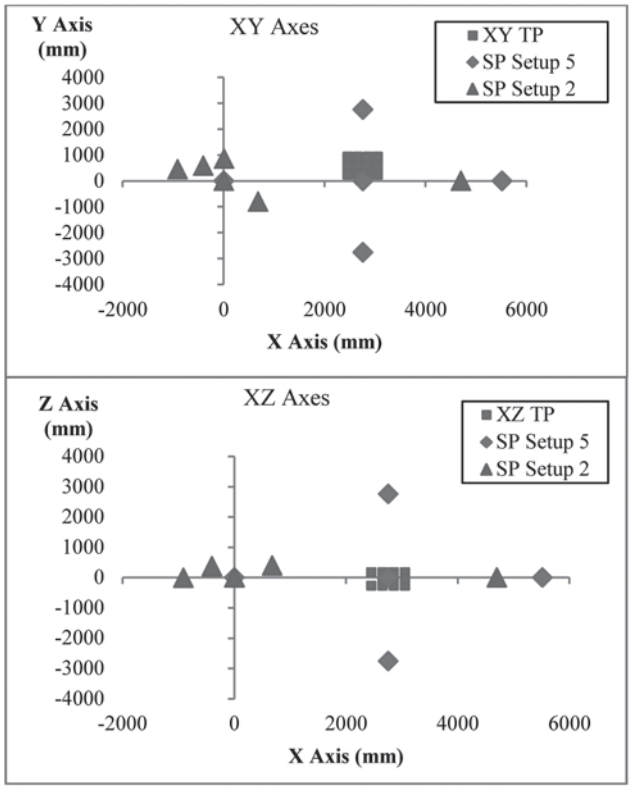

Figure 8: Different Configurations for the Simulations

During the experiment, only two of the six positions were elevated in Z direction, with only about 350 mm. In comparison the positions spanned the X axis with 5 m and the Y axis with 1,2 m. Basically, it gives more information for the solver in the X and Y directions, leaving more uncertainty in Z axis. This consideration is further motivated by [13,15,16]. Based on this, simulations were made which replicate the experimental setup and other configurations, for simulation verification and configuration improvement purposes. Figure 8 shows two of the five different configuration setups used. Note that setup 2 is similar to the test configuration.

Figure 9 depicts the average deviation for the different configurations for the simulations. This was obtained through taking the absolute of the average of 5000 Monte Carlo iterations for each setup. This result gives evidence that the simulation obtains the same type of error for a configuration similar to test setup. It also confirms that the configuration affects the obtainable accuracy. Setup 5 is clearly the most ideal configuration, of the five used. This setup however is not practically feasible, if a corner cube type retroreflector is used, due to the acceptance angle limitation of this type of target. A cat's eye retroflection however can reduce this constraint [17].

The number, location and configuration of the TP and the number of tracker locations used for the positional self-calibration will also affect the accuracy of the program. This can be simulated with the program. See [13,15,16] for guidelines on calibration configuration selection.

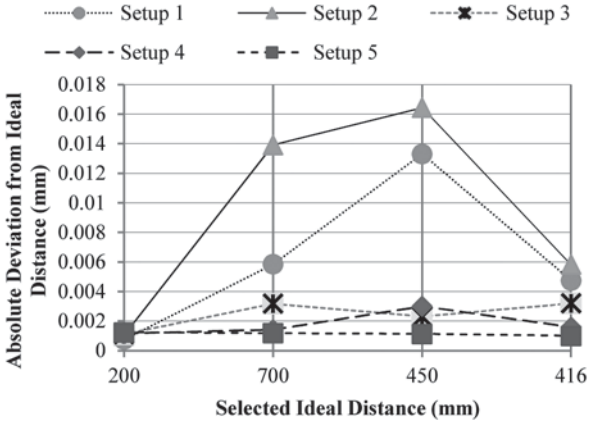

Figure 9: Average Deviation for the Different Configurations

5. MULTILATERATION SIMULATION

Simulations were done to investigate if the program can improve on the result obtained by a laser tracker or the average of multiple trackers. It was assumed that a sufficient number of trackers were available for these simulations.

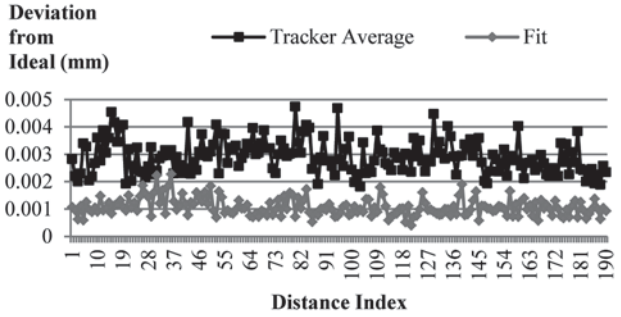

Figure 10: Average Deviation from Ideal Distance for Fit and Simulated Tracker Measurements

Figure 10 is a graph comparing the average of ten iterations of the simulation program, with six tracker stations arranged as setup 5 measuring simultaneously. All possible distances in a 20 point array were calculated and compared.

A 37% improvement on average is found and this illustrates the benefit of multilateration. The three dimensional distance comparison does give a better indication to the accuracy of the system variables than the final cost. The accuracy of the fit system variables compared against the tracker and tracker average measured values however still needs to be investigated.

6. CONCLUSION

A laser tracker is a highly accurate measuring instrument, with many applications in the coordinate measurement

field. The concept of multilateration is able to even further improve this accuracy. The multilateration and simulation program which was developed and can be used by the Dimensional Lab to further study multilateration in the future. The prototype also gave insight into tracker station requirements.

Multilateration however is complex to implement with the optimisers' dependence on initial values and system configuration. Other accuracy constraints are the beam steering mechanism's dead path error contribution and, if sequential multilateration is used, the repeatability of the target points.

The investigation also found that the final cost at the local minimum is not a sufficient indication of whether the solver found a good fit for the measured data. Another comparison is needed, for example three dimensional distances or absolute point coordinates.

Future work will be to investigate a third comparison method, by comparing actual target points and tracker station locations, with the measurements and the fit result. Improving the non-linear least square algorithm by using weightings will be investigated. Furthermore, additional tests will be performed and the feasibility to calibrate a conventional bridge type CMM will be investigated.

7. ACKNOWLEDGEMENTS

The author thanks F van der Walt for helping with CMM and laser tracker measurements, the Mechatronic Engineering Department of the University of Stellenbosch and Prof. K Schreve, for supervising this project.

8. REFERENCES

[1] Benjamin B. Gallagher, "Optical shop applications for laser tracking metrology systems," Department of Optical Sciences, University of Arizona, 2003.

[2] T. Takatsuji, M. Goto, T. Kurosawa, and Y. Tanimura, "The first measurement of a three-dimensional coordinate by use of a laser tracking interferometer system based on trilateration," *Measurement Science and Technology*, vol. 9, pp. 38-41, 1998.

[3] M. Franke, J. Hannaford and H. Kunzmann H. Schwenke, "Error mapping of CMMs and machine tools by a single tracking interferometer," *CIRP Annals - Manufacturing Technology*, vol. 54, no. 1, pp. 475-478, 2005.

[4] Kam C Lau and Robert J Hocken, "Three and five axis laser tracking systems," Patent 1987.

[5] M. Vincze, JP Prenninger, and H. Gander, "A Laser Tracking System to Measure Position and Orientation of Robot End Effectors Under Motion," *The International Journal of Robotics Research*, vol. 13, p. 305, 1994.

[6] Antonietti N, Giugni A, Pisani M, and Zucco M, "Absolute Distance Meauserement with Sub-Fringe Resolution," in *International Conference on Space Optics*, Rhodes, Greece, 2010.

[7] Umetsu K, Furutani R, Takatsuji T, Osawa S, and Kurosawa T, "Calibration of a CMM using a laser tracking system," in *XVII IMEKO World Congress*, Dubrovnik, Croatia, 2003, pp. 1860-1863.

[8] EB Hughes, A Wilson, and GN Peggs, "Design of a High-Accuracy CMM Based on Multi-Lateration Techniques," *CIRP Annals - Manufacturing Technology*, vol. 49, pp. 391-394, 2000.

[9] GP Greeff, "A study for the development of a laser tracking system utilizing multilateration for high accuracy dimensional metrology," Stellenbosch University, Mechanical and Mechatronic Engineering Department, Master's Thesis 2010.

[10] P.D. Lin, C.H. Lu, and others, "Modeling and sensitivity analysis of laser tracking systems by skew-ray tracing method," *Journal of Manufacturing Science and Engineering*, vol. 127, p. 654, 2005.

[11] H. Zhuang and Z.S. Roth, "Modeling Gimbal Axis Misalignments and Mirror Center Offset in a Single-Beam Laser Tracking Measurement System," *The International Journal of Robotics Research*, vol. 14, p. 211, 1995.

[12] Shui H. Motaghedi, Zvi S. Roth and Ying Bai Hanqi Zhuang, "Calibration of multi-beam laser tracking systems," *Robotics and Computer-Integrated Manufacturing*, vol. 19, no. 4, pp. 301-314, August 2003 2003.

[13] G.X. Zhang et al., "A Study on the Optimal Design of Laser-based Multi-lateration Systems," *CIRP Annals - Manufacturing Technology*, vol. 52, pp. 427-430, 2003.

[14] Y. Bai, H. Zhuang, and ZS Roth, "Fuzzy logic control to suppress noises and coupling effects in a laser tracking system," *IEEE Transactions on Control Systems Technology*, vol. 13, pp. 113-121, 2005.

[15] T. Takatsuji, M. Goto, A. Kirita, T. Kurosawa, and Y. Tanimura, "The relationship between the measurement error and the arrangement of laser trackers in laser trilateration," *Measurement Science and Technology*, vol. 11, pp. 477-83, 2000.

[16] D. Zhang, S. Rolt, and P.G. Maropoulos, "Modelling and optimization of novel laser multilateration schemes for high-precision applications," *Measurement Science and Technology*, vol. 16, pp. 2541-2547, 2005.

[17] L. Guoxiong, Z. Zhen, L. Yongbing, "An improved cat's-eye retroreflector used in a laser tracking interferometer system," *Measurement Science and Technology*, vol. 14, no. 6, pp. 34-40, 2003.

Notes